Dalitz-plot analysis of the 16.62, 17.76, and 18.35 MeV resonances of ^{12}C

Author
Kristian Lytje

Supervisor
Hans O. U. Fynbo

Department of Physics and Astronomy
Aarhus University

June 2021

Abstract

This thesis presents the first detailed Dalitz-plot analysis of the triple-alpha breakup of the 17.76 MeV resonance in ^{12}C, and also somewhat shorter analyses of the nearby 16.62 MeV and 18.35 MeV resonances. The data was taken at the 5 MeV accelerator at Aarhus University, which uses the $^{11}\mathrm{B}(\mathrm{p},\alpha)\alpha\alpha$ reaction to populate the resonances. A sequential two-step model which accounts for interference between multiple partial waves is used to fit the Dalitz plots themselves with simulations. Furthermore, an angular correlation analysis is performed on only the 17.76 MeV resonance. Both analyses agrees on the result: the level is dominated by a 2^- resonance. The analysis for the other two levels are in agreement with previous studies.

Contents

1 Introduction

In the interior of the most massive of stars, three α-particles are constantly being fused into carbon-12. The energy released by this reaction counteracts the endless pressure from the colossal weight of the envelope, creating equilibrium, at least for a time. Due to changes in its composition, gravity eventually wins this tug of war, and the star meets a violent end, scattering its carbon into deep space. This process has been repeated so many times that carbon has become the fourth most abundant element by mass, with ^{12}C its most common form. With so much carbon available, it has become a fundamental building block of all known life; so essential that we can hardly imagine existence without it.

Since some of the first research on ^{12}C was carried out at the Cavendish Laboratory [1][2] almost 85 years ago, it has been the subject of countless other studies. From the prediction and following discovery of the Hoyle state [3][4] which is so essential for stellar nucleosynthesis, to current medicinal studies of its uses in proton therapy [5] - its relevance cannot be understated. We will in this thesis work primarily with the 17.76 MeV 0^+ resonance along with its immediate neighbours, the 16.62 MeV 2^- and 18.35 MeV 3^- resonances. Due to its lower energy and larger cross section, most of the early studies were on the lower-lying 2^- resonance, and primarily in determining its branching ratio to ^{8}Be. It was only later that the 0^+ resonance started receiving attention, and that mostly in the form of larger surveys of the continuum of states in the area. Thus this thesis is one of the first to examine it in greater detail.

1.1 Brief review of the resonances

Since the binding energy of a proton in ^{12}C is 15.96 MeV, levels above this threshold can easily be reached by bombarding ^{11}B with protons. Specific states, such as the 17.76 MeV resonance, can then be formed by tuning the proton beam energy. Since these resonances are all located well above the triple-α threshold of 7.27 MeV, in a sequential picture one decay path will proceed through an intermediate ^{8}Be resonance. Based on the energetics of this reaction, the intermediate resonance can either be the ground state $^{11}\mathrm{B}(\mathrm{p},\alpha_0)^8\mathrm{Be}$ (α_0 channel) or the first excited state $^{11}\mathrm{B}(\mathrm{p},\alpha_1)^8\mathrm{Be}^*$ (α_1 channel). The basic idea is then to use properties of the measured 3α final state, such as its momentum distribution, to deduce properties of the initial ^{12}C resonance. See figure 1 for an overview of the energies involved.

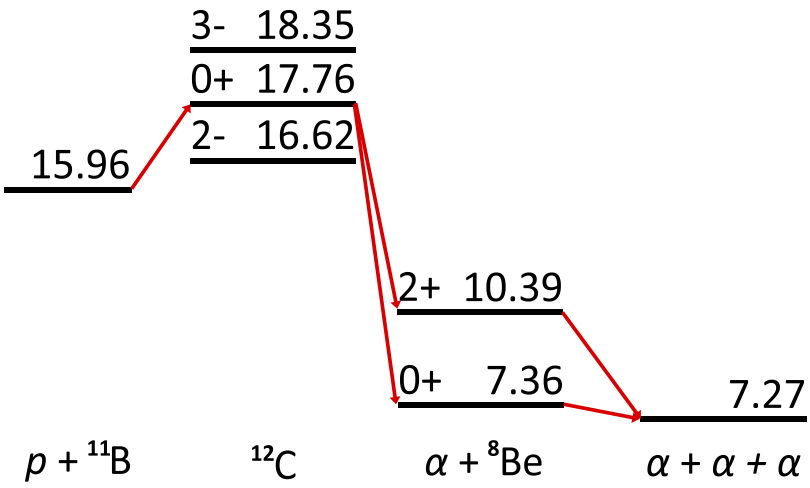

Figure 1: The energetics of the $^{11}\mathrm{B}(\mathrm{p}, 3\alpha)$ reaction.

The 16.62 MeV resonance is the easiest of the three to reach, since it only requires beam energies of around 670 keV. Combined with its larger cross-section, it was an obvious target for the early studies. Due to its unnatural parity, transitions through the α_0 channel are not allowed. Thus its decays can proceed only through the α_1 channel, in which both angular momentum $l = 1$ and $l = 3$ are allowed. One would then expect the $l = 1$ component to dominate due to the angular momentum barrier. However, this is not what Quebert and Marquez [6] found in 1969: they found that their data could only be described if $l = 3$ was the primary decay. Almost twenty years later, Becker, Rolfs and Trautvetter [7] reached the opposite conclusion. A recent study by Stave et al. [8] then reached the same conclusion as Quebert and Marquez. This back-and-forth has been discussed extensively by Kuhlwein [9], who found that the contradictory results are due to differences in the nuclear models and using one-dimensional projections of the two-dimensional phase-space distribution. By allowing both components into a single fit to the full distribution, they found that a mix of about 80% $l = 1$ and 20% $l = 3$ to best fit their data.

The 17.76 MeV resonance has not received quite as much attention throughout the years, and what studies did include it has mainly been broad surveys of the continuum of nuclear levels in the area. One of the earliest studies of this type was performed by Symons and Treacy back in 1963 [11], who, based on a Legendre series fit to its angular distribution, labeled it as a 0^+ state. Two years later, a study by Segel et al. [12] supported this assignment, but also noted that they saw a substantial a_3 component, indicating

interference from possibly the nearby 18.35 MeV 3^- resonance. Both studies found the state to be resonant on both the α_0 and α_1 bands, indicating that it must have natural parity - these observations are supported by later studies [13][14]. They also both argue that there are two possible solutions for the branching ratio to these two bands, where Symons and Treacy favors the smaller solution of $\Gamma_{\alpha_0}/\Gamma_{\alpha_1} = 0.209$, while Segel favors the larger solution of 0.403. The NNDC [15] has adopted the latter as its standard value.

The 18.35 MeV resonance shares a similar history with the 17.76 MeV due to their high >2 MeV beam energy requirement. One of its first mentions was in a study of the angular distribution of gamma rays by Gove and Paul in 1955 [10], who tentatively labeled it as a 2^+ state, but noted that this could possibly be due to interference from other nearby states. A few years later, the study by Symons and Treacy [11] reached the same conclusion, although they decisively labeled it as a 2^+ state. It was only during the study by Segel et al. [12] that it received its current classification as a 3^- state, which was later supported by Hanna et al. [13]. Similarly to the 17.76 MeV resonance, there are also here two solutions for its branching ratio to the α_0 and α_1 bands. Once again Symons and Treacy favors the smaller solution of $\Gamma_{\alpha_0}/\Gamma_{\alpha_1} = 0.120$, while Segel favors the larger solution of 0.367. The NNDC again chose the latter as its standard value.

Since Kuhlwein [9] was so successful in describing the 2^- resonance, our goal here is to use the same statistical methods to describe the other two neglected resonances. To our knowledge, we will be the first to perform such a detailed analysis of their Dalitz plots.

2 Theory

Atomic nuclei are bound systems of protons and neutrons which, in our current understanding, are built of quarks and gluons interacting through the laws of quantum chromodynamics. Thus we already have the recipe to describe any nuclear reaction: simply use QCD to calculate the interaction. It is, however, only a select few observables in very specific situations which can be described at such a fundamental level. Thus one of the primary goals of nuclear physics is to develop approximate models which captures the essence of these subatomic interactions, and are applicable to a more general collection of reactions. Some of the primary observables these models should account for are the masses, shapes, spectra, and decay modes of bound states. This thesis deals exclusively with the last part, i.e. the decay modes of resonances populated by nuclear reactions.

One of the more successful models of these interactions is the R-matrix theory, which will be introduced here in this section. We will also devote some time to discussing the kinematics of a sequential decay, and how the correlation angle factors into this.

2.1 The compound nucleus

One of the early theories of nuclear reactions is the idea of a compound nucleus as proposed by Bohr in 1936 [16]. The basic idea is that the incident nucleus is momentarily captured by the target, thus creating an intermediate compound state. The energy of the incident nucleus is then redistributed throughout this compound state due to internal interactions. Central to this description is the idea that the formation and decay of the compound nucleus occurs *independently* of each other.

Further work on the model proved to be very successful, yet also unsatisfactory: it depends on the Weisskopf-Wigner theory of resonance absorption and subsequent emission of radiation [17], and through that, on time-dependent perturbation theory. This is problematic as the nuclear forces can certainly not be treated as mere perturbations. The solution to this problem eventually led to the development of the R-matrix theory, which is the topic of the next section.

2.2 R-matrix theory

This whole section on R-matrix theory follows the general steps used in the lecture notes by Baye [18].

Consider the potential scattering of some arbitrary partial wave. A core assumption of R-matrix theory is that the potential V only differs from the Coulomb potential V_C by a short-range term, such that

$$V(r) \xrightarrow[r\to\infty]{} V_C(r) = \frac{Z_1 Z_2 e^2}{4\pi\epsilon_0 r}$$

The central idea of the theory is that beyond some specific radius $r = a$, the short-range term can be neglected. Thus this interaction radius a effectively divides space into two regions: an internal region, where the nuclear interactions must be accounted for, and an external region, where only the Coulomb interaction matters. The internal region is treated as a confined system, allowing the total wave function to be expanded into a finite set of eigenstates. In the external region, the wave function can be approximated by its asymptotic value, leaving only an unknown phase shift. By matching the two wave functions at the boundary, this phase shift can be identified.

2.2.1 The internal and external wave functions

Assume that we have two particles with the reduced mass μ, which interacts through the central potential V with some positive energy

$$E = \frac{\hbar^2 k^2}{2\mu}$$

By applying the Schrödinger equation to this situation, we get

$$\left(-\frac{\hbar^2}{2\mu}\Delta + V(r) \right)\psi(\boldsymbol{r}) = E\psi(\boldsymbol{r})$$

Since we are dealing with a central potential, the wave function can be factorized into its radial and spherical components

$$\psi(r,\theta,\phi) = R_l(r)Y_l^m(\theta,\phi) \tag{1}$$

Note that in contrast to the usual factorization, R_l also depends on the orbital angular momentum l since we are still dealing with only a single partial wave.

To simplify matters a bit, we make the change of variables $u(r) = rR(r)$, such that (1) becomes

$$\psi(r, \theta, \phi) = \frac{u_l(r) Y_l^m(\theta, \phi)}{r}$$

This allows us to write the radial part of the Schrödinger equation as

$$\left[-\frac{\hbar^2}{2\mu} \left(\frac{d^2}{dr^2} + \frac{l(l+1)}{r^2} \right) + V(r) \right] u_l(r) = E u_l(r)$$

Defining everything on the left-hand side as the Hamiltonian H_l, the equation can be restated more simply as

$$(H_l - E) u_l = 0 \tag{2}$$

We are interested in the normalizable bounded radial solutions u_l of (2), so we must require that $u_l(0) = 0$. The positive energy solutions to this have the asymptotic behaviour

$$u_l(r) \xrightarrow[r \to \infty]{} F_l(\eta, \rho) \cos \delta_l + G_l(\eta, \rho) \sin \delta_l \tag{3}$$

where F_l and G_l are the regular and irregular Coulomb functions, and δ_l the Coulomb phase shift. The arguments to the Coulomb functions are $\rho = kr$ and the Sommerfeld parameter $\eta = Z_1 Z_2 e^2 / 4\pi\epsilon_0 \hbar v$, with $v = \sqrt{2E/\mu}$ the relative velocity of the interacting nuclei. It can be shown that the two Coulomb functions satisfies the Wronskian (temporarily suppressing ρ and η) $F_l' G_l - G_l' F_l = 1$, which will be useful later.

Another possible solution is given as

$$u_l(r) \xrightarrow[r \to \infty]{} I_l(\eta, \rho) - U_l O_l(\eta, \rho) \tag{4}$$

where $I_l = G_l - iF_l$ and $O_l = G_l + iF_l$ are the incoming and outgoing Coulomb functions, and U_l the scattering matrix defined by

$$U_l = e^{2i\delta_l}$$

As per the base assumption of R-matrix theory, we can approximate the radial wave function u_l^{ext} in the external region with the two solutions (3) and (4). The other base assumption allows us to expand the radial wave function u_l^{int} for the internal region over some finite basis of linearly independent functions φ_j:

$$u_l^{\text{int}}(r) = \sum_j^N c_j \varphi_j(r) \tag{5}$$

To ensure that the total wave function u_l vanishes at the origin, so too must all φ_j. Although they are not strictly required to be orthogonal at this stage, we will assume they are for later use. Neither are they required to satisfy any specific boundary condition at $r = a$. Instead, continuity of the total wave function u_l and its first derivative across the boundary will be used to connect the internal and external wave functions.

2.2.2 Bloch operator

At this stage, a major issue becomes apparent: the Hamiltonian H_l is not Hermitian in the internal region:

$$\begin{aligned}\int_0^a f H_l g dr - \int_0^a g H_l f dr &= \left(-\frac{\hbar^2}{2\mu}\right)\left[\int_0^a f\frac{d^2}{dr^2}g dr - \int_0^a g\frac{d^2}{dr^2}f dr\right] \\ &= -\frac{\hbar^2}{2\mu}\Big(f(a)g'(a) - g(a)f'(a)\Big) \qquad (6)\end{aligned}$$

Bloch [19] neatly solved this issue by introducing a new surface operator

$$\mathcal{L} = \frac{\hbar^2}{2\mu}\delta(r-a)\frac{d}{dr}$$

The operator is specifically designed to cancel (6), as can be seen by repeating the calculation:

$$\begin{aligned}\int_0^a f\mathcal{L}g dr - \int_0^a g\mathcal{L}f dr &= \left(-\frac{\hbar^2}{2\mu}\right)\left[\int_0^a f\delta(r\text{ - }a)\frac{d}{dr}g dr - \int_0^a g\delta(r\text{ - }a)\frac{d}{dr}f dr\right] \\ &= \frac{\hbar^2}{2\mu}\Big(f(a)g'(a) - g(a)f'(a)\Big)\end{aligned}$$

Thus when combined with the Hamiltonian, the total operator $H_l + \mathcal{L}$ *is* Hermitian. This new combined operator allows us to approximate the Schrödinger equation for the internal region by the Bloch-Schrödinger equation

$$(H_l + \mathcal{L} - E)u_l^{\text{int}} = \mathcal{L}u_l^{\text{int}} \qquad (7)$$

This equation turns out to be equivalent to (see e.g. [18])

$$(H_l - E)u_l^{\text{int}} = 0 \qquad\qquad u_l^{\text{int}\prime}(a) = u_l^{\text{ext}\prime}(a)$$

that is, the original Schrödinger equation (2) confined to the internal region, along with the first half of our continuity condition for the total wave function. Thus by supplementing it with the other half

$$u_l^{\text{int}}(a) = u_l^{\text{ext}}(a)$$

the Bloch operator guarantees continuity of the total wave function and its first derivative across the boundary.

2.2.3 The calculable R-matrix

The namesake of the theory is defined by the equation

$$u_l(a) = R_l(a, E) a u_l'(a) \tag{8}$$

Thus its inverse

$$R_l^{-1}(a, E) = a \frac{u_l'(a)}{u_l(a)}$$

is the logarithmic derivative of the radial wave function evaluated at the boundary. So far, we have completely avoided one of the core concepts of R-matrix theory: channels. These channels corresponds to different projectile-target combinations, channel spins, and relative angular momenta. The R-matrix in the above equation is just a number; it relates one input channel to one output channel. In general, it will be a matrix containing an entry relating each pair of input and output channels. To obtain another representation of the matrix, the basis expansion of the internal wave function (5) is applied to the Bloch-Schrödinger equation (7), and subsequently projected onto the basis $\varphi_i(r)$:

$$\sum_j^N \langle \varphi_i | H + \mathcal{L} - E | \varphi_j \rangle c_j = \frac{\hbar^2}{2\mu} \varphi_i(a) u_l^{\text{ext}\prime}(a) \tag{9}$$

The right-hand side follows directly from the Bloch-Schrödinger equation along with the continuity condition. To simplify matters a bit, it is here convenient to introduce the symmetric $\boldsymbol{C}$-matrix

$$\boldsymbol{C}_{ij}(E) = \langle \varphi_i | H + \mathcal{L} - E | \varphi_j \rangle$$

By solving equation (9) for the expansion coefficients c_j, we get the equation

$$c_j = \frac{\hbar^2}{2\mu} u_l^{\text{ext}\prime}(a) \sum_i^N (\boldsymbol{C}^{-1})_{ij} \varphi_i(a)$$

We can insert them back into the expansion equation (5) and compare with the first equation for the R-matrix (8) to get an equation for the calculable R-matrix

$$R_l(a, E) = \frac{\hbar^2}{2\mu a} \sum_{i,j}^N \varphi_i(a) (\boldsymbol{C}^{-1})_{ij} \varphi_j(a) \tag{10}$$

To complete this definition of R, we thus need to invert the C-matrix. To do this, we will finally need the orthonormality of the basis functions $\varphi_i(r)$. Remember that $\boldsymbol{C}$ implicitly depends on the energy E. Consider its non-zero eigenvalues E_{nl} and corresponding eigenvectors $\boldsymbol{v}_{nl}$ evaluated for $E = 0$

$$\boldsymbol{C}(0)\boldsymbol{v}_{nl} = E_{nl}\boldsymbol{v}_{nl}$$

with the orthonormality condition $\boldsymbol{v}_{nl}^T\boldsymbol{v}_{nl} = \delta_{nn'}$. The requirements listed here are exactly what we need to invert it through its eigendecomposition, where the inverse is given as

$$\boldsymbol{C}(0)^{-1} = \sum_n^N \frac{\boldsymbol{v}_{nl}\boldsymbol{v}_{nl}^T}{E_{nl}}$$

This can easily be modified to work for any non-zero energy E: simply subtract it from the denominator, such that

$$\boldsymbol{C}(E)^{-1} = \sum_n^N \frac{\boldsymbol{v}_{nl}\boldsymbol{v}_{nl}^T}{E_{nl} - E} \tag{11}$$

Before we get to one of the primary results of R-matrix theory, there is a minor detail that should be corrected. So far we have worked with a finite basis, and thus everything is only approximately correct. To fix this issue, we can simply let N tend toward infinity in all our sums. Going on with the derivation, we can now insert (11) into our previous equation for the R-matrix (10) to get the equation

$$\begin{aligned} R_l(E) &= \frac{\hbar^2}{2\mu a}\sum_{i,j}^{\infty}\varphi_i(a)\left(\sum_n^{\infty}\frac{\boldsymbol{v}_{nl}\boldsymbol{v}_{nl}^T}{E_{nl} - E}\right)_{ij}\varphi_j(a) \\ &= \sum_n^{\infty}\frac{\gamma_{nl}^2}{E_{nl} - E} \end{aligned}$$

where γ_{nl} is defined as

$$\gamma_{nl} = \sqrt{\frac{\hbar^2}{2\mu a}}\sum_i^{\infty}\boldsymbol{v}_{nl,i}\varphi_i(a) \tag{12}$$

γ_{nl} is known as the reduced width amplitude. It received this name since its square is a crucial component of the total width, as we will see in a moment.

In general, the R-matrix has an infinity of real simple poles. If we instead approximate the solution, such that we only deal with a small number of poles, we will eventually arrive at the *phenomenological* R-matrix. More specifically, if we approximate the matrix by a single pole with energy E_1 and reduced width γ_{1l}^2, one can derive the equation (see e.g. [20])

$$\Gamma = \frac{2\gamma_{1l}^2 P(E_R)}{1 + \gamma_{1l}^2 S'(E_R)} \tag{13}$$

which relates the total width Γ to the reduced width γ_{1l}^2. Here $P(E_R)$ and $S'(E_R)$ are the penetrability and shift function, which will both be introduced in the next section. This equation will be relevant later when we want to compare simulations from different reaction models.

2.2.4 Determining the Coulomb phase shift

One of our first applications of the theory is to determine the Coulomb phase shift δ_l and the collision matrix U_l from (3) and (4), respectively. Since we have already derived all of the necessary tools, this is simply a matter of substituting the two equations into the definition of the R-matrix (8). Throughout this section, all function dependencies will be suppressed for clarity, so remember that all of the Coulomb functions are evaluated at the boundary $\rho = ak$.

For the phase shift, we obtain the equation

$$F_l \cos\delta_l + G_l \sin\delta_l = \rho R_l \left[F_l' \cos\delta_l + G_l' \sin\delta_l\right]$$

By solving for the phase shift δ_l, we get the equation

$$\tan\delta_l = -\frac{F_l - \rho R_l F_l'}{G_l - \rho R_l G_l'}$$

We can repeat the exact same calculations for the scattering matrix to get the equation

$$U_l = \frac{I_l - \rho R_l I_l'}{O_l - \rho R_l O_l'} = e^{2i\phi_l}\frac{1 - L_l^* R_l}{1 - L_l R_l} \tag{14}$$

The third term is obtained through some tedious calculations by defining the logarithmic derivative of O_l at the channel radius, along with the hard-sphere phase shift ϕ_l as

$$L_l = \rho\frac{O_l'}{O_l} \qquad\qquad \phi_l = -\arctan\frac{F_l}{G_l}$$

The meaning of these two equations are not that relevant for this discussion. It is worth noting that L_l is typically an imaginary number, and so it is often split into its real and imaginary parts as

$$L_l = S_l + iP_l$$

where S_l and P_l are called the shift and penetrability factors. Through the definition of L_l and the Wronskian relation satisfied by the Coulomb functions F_l and G_l, a short derivation (see appendix A.1) gives the equations for P_l and S_l as

$$P_l = \frac{\rho}{F_l^2 + G_l^2} \qquad\qquad S_l = \rho \frac{F_l F_l' + G_l G_l'}{F_l^2 + G_l^2} \tag{15}$$

These two equations are used internally in our width converter tool, which will be introduced later.

2.2.5 Three-body decays

So far, the R-matrix theory can only describe two-body decays. To extend the model to also cover three-body decays, we assume that the decay occurs sequentially, i.e. $^{12}\mathrm{C} \rightarrow {}^{8}\mathrm{Be} + \alpha \rightarrow 3\alpha$. The idea is then that we can use the standard R-matrix model to describe the first decay of a definite initial input ^{12}C channel to all possible intermediate ^{8}Be channels. We can then again use the standard model to describe each decay from the channels of ^{8}Be to the definite final output channel 3α.

By using these extensions, one can derive similar equations as for the two-body model, which will not be discussed here. This sequential three-body model is used internally in some of the simulation tools which will be introduced later.

2.3 Kinematics

We will later have need of some basic kinematic results for a sequential decay, which will be introduced in this section. A useful way of visualizing three-body decays will also be introduced.

2.3.1 Basic results

If we define all our energies with respect to the ground state of ^{12}C, we can write the energy released in the first and second decay step as $Q_1 = E_{^{12}\mathrm{C}} - E_{^{8}\mathrm{Be}}$ and $Q_2 = E_{^{8}\mathrm{Be}} - E_{3\alpha}$, respectively. The first α particle to be

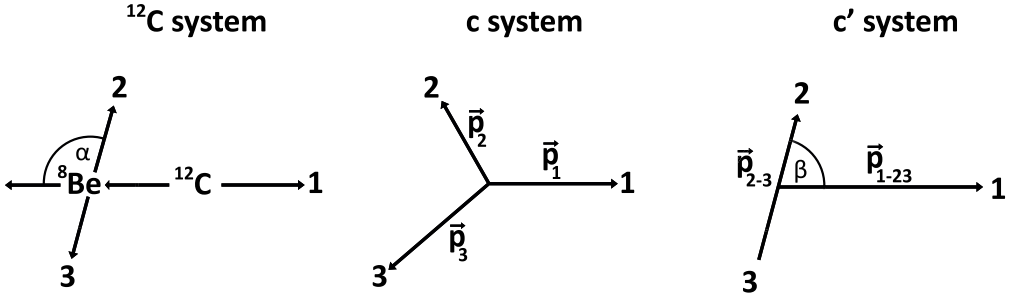

Figure 2: Three frames of the same reaction. The left panel is the standard center-of-mass frame for ^{12}C. The middle panel illustrates the same frame using momentum vectors. The right panel shows the sequential decay relative coordinate c' system where particle 1 is always defined as the primary. These last two frames are both defined as in [21].

emitted from the ^{12}C decay is called the *primary* particle, while those from the ^{8}Be decay are called *secondary*. The energies of the individual α-particles can then be calculated through conservation laws to be (see appendix A.2)

$$E_1 = \frac{2}{3}Q_1 \tag{16}$$

$$E_2 = \frac{1}{6}Q_1 + \frac{1}{2}Q_2 + \cos\alpha\sqrt{\frac{Q_1Q_2}{3}} \tag{17}$$

$$E_3 = \frac{1}{6}Q_1 + \frac{1}{2}Q_2 - \cos\alpha\sqrt{\frac{Q_1Q_2}{3}} \tag{18}$$

where α is the angle between the axis defined by the first decay and the second α-particle, see figure 2. As this angle will be important later, it is worthwhile to isolate this quantity:

$$2\cos\alpha = \sqrt{\frac{3}{Q_1Q_2}}(E_2 - E_3) \tag{19}$$

A few other relevant properties of 3-particle reactions are presented in [21]. From this paper, especially the excitation energy of the particle 2-3 system E_{2-3} is important, since it is simply the excitation energy of ^{8}Be. Thus it gives us a powerful method of distinguishing decays through the α_0 and α_1 channels. For our triple-α decay, the quantity is defined as

$$E_{2-3} = \frac{p_{2-3}^2}{2\mu} = \frac{(\boldsymbol{p}_2 - \boldsymbol{p}_3)^2}{4m_\alpha} \tag{20}$$

Another quantity introduced in the same paper is the breakup angle β, defined as

$$\cos\beta = \frac{\boldsymbol{p}_{1-23} \cdot \boldsymbol{p}_{2-3}}{p_{1-23} p_{2-3}} \tag{21}$$

As can be seen on figure 2, the two angles α and β both describes the correlation angle between the primary and secondary particles. The reason we have introduced two different ways of determining this angle will become clear in the next section - the explanation is basically that they are used in two different areas of the analysis.

2.3.2 The Dalitz plot

The goal of this thesis is to understand the excited states of ^{12}C based on the three α-particles resulting from its decay. We can describe each of these decay products with a four-vector, for a total of 12 degrees of freedom. Conservation of energy and momentum removes four degrees, the three masses m_α removes three, and finally the orientation of each product removes another three. Thus we are left wondering how best to choose the two remaining degrees of freedom.

A popular choice in nuclear and particle physics are the Dalitz coordinates

$$x = \sqrt{3}\frac{E_2 - E_3}{E_{tot}} \qquad\qquad y = \frac{3E_1}{E_{tot}} - 1 \tag{22}$$

devised by Dalitz back in 1953 [22]. With these coordinates, each of the measured three-body final states are represented by a single point in a 2D histogram. Energy and momentum conservation restricts these points to fall within an equilateral triangle and an inscribed circle, respectively. It can be shown that within these areas, the phase space volume is constant [23], such that any structure which may arise is due to properties of the reaction itself. An illustration of this type of plot can be seen on figure 3.

Since we are dealing with three identical bosons, we are free to label them however we please. This introduces a six-fold symmetry to our Dalitz plots, which can be realized by defining one specific order, e.g. $E_1 \geq E_2 \geq E_3$. This ordering makes all events fall within the hatched area on figure 3. Although this single slice contains all the information of the decay, since it is easier to see structure on the full plot, we will mainly be using those.

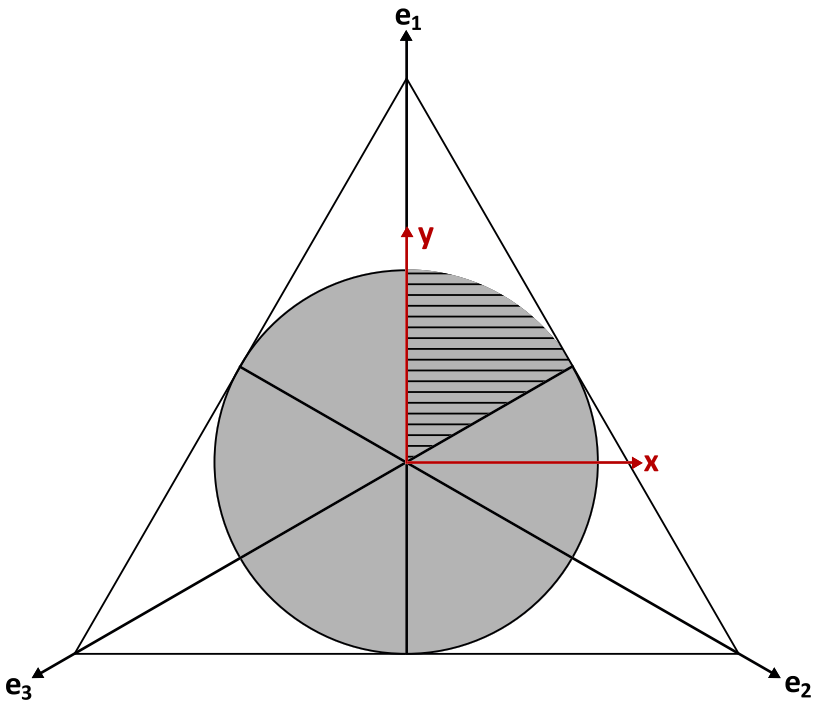

Figure 3: The Dalitz plot showing both the Dalitz coordinates (22) and the normalized energy coordinates (16) to (18). The triangle and circle defines the regions allowed by energy and momentum conservation, respectively. By ordering the energies such that $E_1 \geq E_2 \geq E_3$, all events must fall within the hatched area.

Further studies on the effects of symmetries in Dalitz plots were performed by Zemach in 1964 [24], where it was shown that some areas of the plot are suppressed, depending on properties of the parent state. Although the study was for triple pion decay, it is just as applicable for our α decay. The suppressed regions are shown on figure 4. Although no restrictions are imposed on our 0^+ resonance, it will be useful for the other two 2^- and 3^- resonances.

The equation for the angle between the primary and secondary particles, α, is given in the $\{e_1, e_2, e_3\}$ coordinate system through (19). Since we will be dealing exclusively with the Dalitz coordinates, it is useful to convert this to an equation of $\{x, y\}$ instead. A simple exercise (see appendix A.2) gives the solution as

$$\cos\alpha = \frac{x}{\sqrt{1-y^2}} \tag{23}$$

Since it depends on neither Q_1 nor Q_2, the angular distribution of the particles is common to all Dalitz plots, and can be seen on the left panel in figure

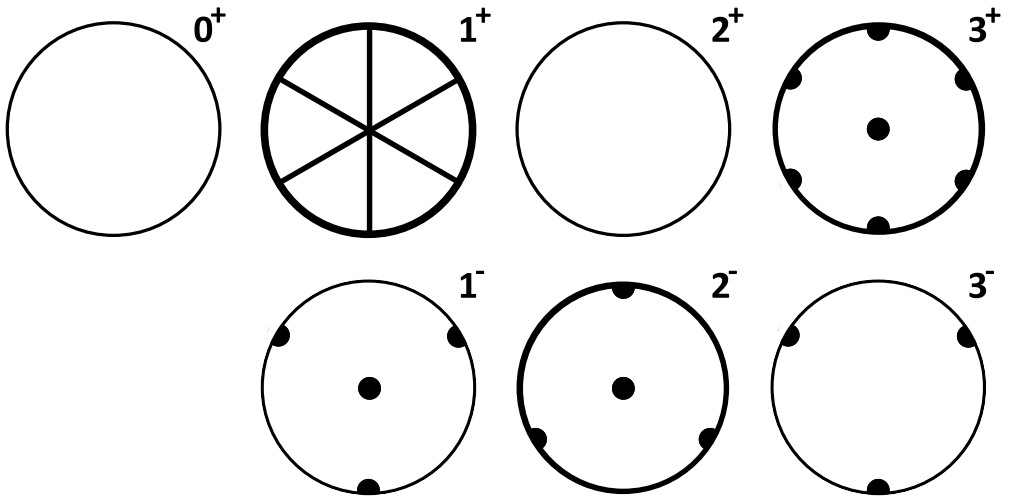

Figure 4: Suppressed regions of the 3α Dalitz plot, as required by Zemach's [24] analysis. Solid black lines and points indicates the suppressed areas. Only the states relevant for this thesis are shown here. The figure is based on the work of [25].

5. The right panel shows the angle for a select few values of y. This also illustrates why both equation 19 and 21 are relevant: one can be extracted directly from the Dalitz plot through a simple projection onto the x axis, while the other is independent of it. Thus they offer two complementary methods of determining the same angle.

2.4 Angular correlations

Now that we have discussed how to extract the correlation angles from the data, it is time to discuss how we expect them to be distributed.

The formalism used in this thesis follows the work of Biedenharn [26], as explained in appendix D of the book *Nuclear Physics of Stars* [27]. We assume that the beam is unpolarized, and that the nuclear levels involved have unique spin and well-defined parities. The correlation between two decay products can in general be expressed as a series of Legendre polynomials in the angle between them

$$W(\beta) = \frac{1}{b_0} \sum_{n=0}^{N} b_n P_n(\cos\beta) \tag{24}$$

Since we assumed that each stage of the reaction has a well-defined parity,

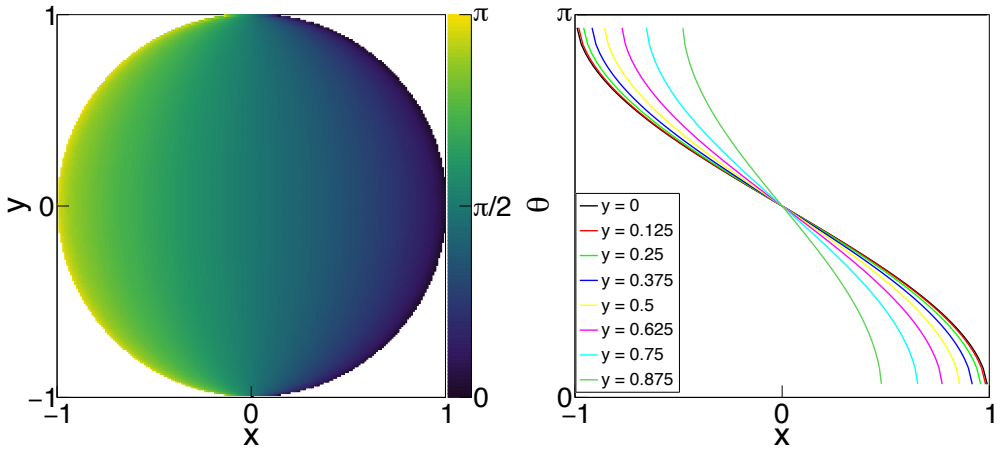

Figure 5: The angle α between the primary and secondary particles. The left panel shows the angle for all points in the Dalitz plot. The right panel shows the projection for a select few values of y, to more clearly show how the angle varies across the plot.

the wave function describing the exit channel must have the same parity as the intermediate state. The intensity of the emitted radiation (square of the wave function) must then always have even parity, meaning it is unchanged by the parity transformation $\mathbf{r} \to -\mathbf{r}$, which we can express in terms of β as $\beta \to \pi - \beta = \alpha$, since the intensity does not depend on the azimuthal angle for unpolarized beams and randomly oriented target nuclei. This condition carries over to the Legendre polynomials, such that we require $W(\beta) = W(\alpha)$, meaning they are all symmetric about $\beta = \pi/2$. This condition is only satisfied by all even polynomials, and so the odd ones must vanish.

The b_n coefficients in (24) will generally depend on the quantum properties of the interacting nuclei. Biedenharn [26] calculated the related coefficients F_n, given as

$$F_n(LL'jJ) \equiv (-1)^{j-J-1}\sqrt{(2L+1)(2L'+1)(2J+1)} \times \langle L1L'-1|n0\rangle W(JJLL';nj)$$

where $\langle L1L'-1|n0\rangle$ and $W(JJLL';nj)$ denotes a Clebsch-Gordan and a Racah coefficient, respectively. The symmetry properties of these coefficients limit how many terms are needed in the sum, as $F_n(LLjJ) \neq 0$ only for $0 < n \leq \min(2J, 2L)$.

In a two-step decay process, the angular correlation can then be written in

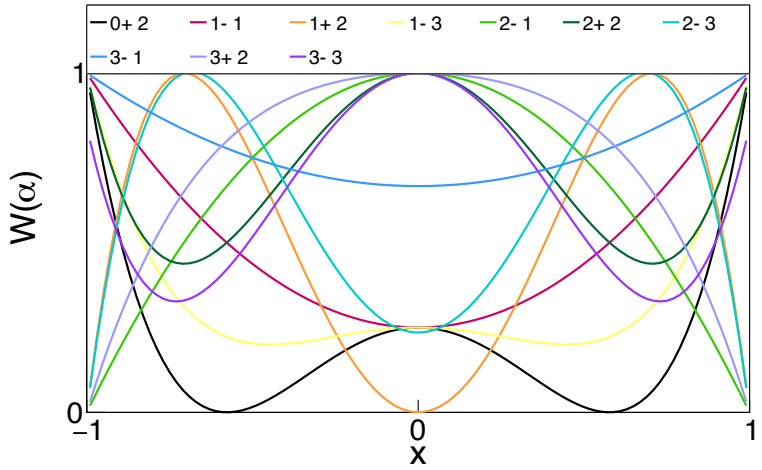

Figure 6: The angular correlation functions for a few different nuclear states and primary angular momenta, plotted in terms of the Dalitz angle α from (23). The legend is of the form $(j_1\pi_1\ l_1)$, where j_1 and π_1 is the angular momentum and parity of the ^{12}C state, and l_1 is the angular momentum carried by the primary α particle.

terms of F_n as

$$W(\beta) = \sum_{n=0,2,\ldots} [a_n(l_1)F_n(l_1 j_1 J)][a_n(l_2)F_n(l_2 j_2 J)]P_n(\cos\beta)$$

where $a_n(l)$ is given as

$$a_n(l) = \frac{2l(l+1)}{2l(l+1) - n(n+1)}$$

and n runs from 0 to $\min(2l_1, 2l_2, 2J)$. l_1 and l_2 are then the angular momenta of the primary and secondary α-particles, while j_1, J, and j_2 are the angular momenta of the initial ^{12}C, the intermediate ^{8}Be, and the final free α state, respectively. Thus for decays to the first excited state of ^{8}Be which we will primarily be working with, $J = 2$, $j_2 = 0$ and $l_2 = 2$, leaving only j_1 and l_1 as free variables that depends on the ^{12}C state. Some examples of these correlation functions can be seen in figure 6, plotted in terms of the Dalitz angle α from (23). Due to its nonlinear dependency on x, the functions are squashed near the borders of the plot.

2.5 Statistics

Suppose we have a set of statistically independent quantities $\boldsymbol{x}$, all distributed with the same probability density function $f(x, \boldsymbol{\theta})$. Here $\boldsymbol{\theta}$ is some arbitrary

set of parameters on which the distribution function depends, which we would like to estimate. One way of doing this is by constructing the likelihood function

$$\mathcal{L}(\boldsymbol{\theta}) = \prod_{n}^{i} f(x_i; \boldsymbol{\theta}) \tag{25}$$

which, roughly speaking, describes the combined probability (or likelihood) of observing $\boldsymbol{x}$ given the density function $f(x, \boldsymbol{\theta})$ for some choice of parameters $\boldsymbol{\theta}$. The basic idea is then that by maximizing this probability, we obtain the best estimate of our parameters $\boldsymbol{\theta}$. Sometimes the number of events n also depends on the parameters. If this is the case, the probability of observing exactly n events should be included in the likelihood. Since we are dealing with Poisson-distributed data, (25) is thus modified to

$$\mathcal{L}(\boldsymbol{\theta}) = \frac{\mu^n}{n!} e^{-\mu} \prod_{n}^{i} f(x_i; \boldsymbol{\theta}) \tag{26}$$

which is often called the extended likelihood.

When we apply this idea to our binned histogram data, the density function $f(x, \boldsymbol{\theta})$ is that of a multinomial distribution. Inserting this into (26) and taking the natural logarithm for numerical stability, we get

$$\ln \mathcal{L}(\boldsymbol{\theta}) = \sum_{i}^{n} \ln \frac{\mu_i}{m_i} + m_i - \mu_i \tag{27}$$

Here μ is the expected number of events in each bin, while m is the observed number. It is thus by maximizing this equation that we obtain the maximum likelihood estimate for our parameters $\boldsymbol{\theta}$.

To obtain a goodness-of-fit test statistic, one can instead minimize the likelihood ratio $-2\lambda = -2 \ln f(\boldsymbol{m}; \boldsymbol{\theta}) / f(\boldsymbol{m}; \boldsymbol{\mu})$, where the denominator is to be understood as the values one would find without any errors. As per Wilk's theorem, this quantity will asymptotically approach a χ^2 distribution with $\mu - \theta$ degrees of freedom. Since $\boldsymbol{\mu}$ is generally unknown, we can replace it by $\boldsymbol{m}$ [31].

The final issue is how to deal with errors. For finite samples, the covariance matrix can result in an underestimate of the variances. A numerically equivalent approach to determine the s-standard deviation confidence interval is

by finding the set of parameters $\boldsymbol{\theta}'$ where

$$\ln \mathcal{L}(\boldsymbol{\theta}') = \ln \mathcal{L}_{max} - s^2/2$$

This will in general result in asymmetrical errors on the parameters. [28]

When we want to fit Monte Carlo simulations to our data, we introduce a statistical uncertainty to the expected number of events μ_i since the values from the simulation are only approximations. To account for this, the maximum likelihood statistic introduced here must be modified as done in [9] and [29].

3 Experiment

The work presented here in this thesis is based on a series of measurements carried out by the 5 MeV accelerator at Aarhus University in 2017. From these, specifically the measurements involving the 17.76 MeV 0^+ resonance of ^{12}C is of interest. Although this section is written from the perspective of the 0^+ resonance, with some minor changes in the numbers, it is equally valid for any of the other resonances.

3.1 Experimental setup

A standard 5 MeV Van de Graaf accelerator is used to generate a 2001 keV proton beam. The beam is then guided through a series of slits before impacting the target nucleus in a reaction chamber. A Faraday cup is placed further downstream to pick up any remnant beam particles. The target is a $\sim$120 nm thick ^{11}B layer on carbon backing.

As already mentioned in the introduction to this section, this setup was also used to measure other nearby excited states of carbon, such as the 16.62 MeV 2^- and 18.35 MeV 3^- resonances. These two sets of measurements will be used mainly to provide some perspective on the results of the 0^+ resonance.

3.1.1 Detectors

Four double-sided silicon-strip detectors (DSSD) from *Micron Semiconductor Ltd* were used; two each of the models W1 and S3. The front side of each detector is p-doped, and is split into a number of strips. Similarly the back side is n-doped, and split into strips running perpendicularly to the front side. Thus these two sets of strips effectively constitutes a grid of pixels, which allows us to sensitively measure the direction of a particle.

When a particle hits a detector, its surface atoms are ionized, and produces electron-hole pairs proportional to the energy of the incident particle. The bias voltage collects the electrons and holes on a pair of aluminum contacts, from which a signal can be measured. Since any energy deposited in the aluminum is lost, it effectively acts as a dead layer for the particles.

The $49.5 \times 49.5\,\mathrm{mm}^2$ surface area of the W1 detectors are split into 16 $3 \times 50\,\mathrm{mm}^2$ rectangular strips on each side, thus creating 256 $9\,\mathrm{mm}^2$ pixels. They are 60 μm thick, and have a dead layer equivalent to 100(10) nm of silicon. They are placed parallel to the beam axis, at a distance of 4 cm. Due

to the symmetry of the setup, it does not matter which names we associate with the left and right side, and they have thus been named simply Det1 and Det2.

The S3 detectors are annular, such that the beam can travel through the central hole. They have an inner radius of 11 mm, and an outer radius of 35 mm. The front side is split into 32 radial spokes, while the back side is split into 24 rings, thus constituting 768 pixels of varying sizes. They are 322 μm thick, and have a dead layer equivalent to 570(57) nm of silicon. The two detectors are both placed perpendicularly with the beam axis, at a separation of 36 mm from the target. The upstream detector is named SU(pstream), while the downstream detector is named SD(ownstream). Due to its downstream position, the inner 16 rings of the SD are covered by a collimator. Furthermore its spokes 1, 2, 3, and 32 have not registered anything, and are most likely broken. All other strips in the other detectors appear to be working correctly.

As can be seen on figure 7, the setup covers a rather large solid angle, which is ideal for measuring multi-coincidence data. This will later allow us to filter the data to only the events where all three decay products were detected. To reduce the amount of data gathered, a trigger with a logical AND condition is used, thus requiring a simultaneous hit in at least two detectors. Furthermore, to reduce the number of detected Rutherford scattered protons, a downscaling is applied to each individual detector: For every four events accepted by the SU, two are accepted in each of the W3's, and only a single event is accepted by the SD due to its downstream position.

The analogue signals from the trigger logic are digitized by the data acquisition system, whose main components can be seen in figure 8. Since the charge is impractically small, the first step is to pass it through a preamplifier, which also shapes the signal into a fast-rising pulse with a rather long tail. The signal is then passed to the amplifier, which further amplifies and shapes the signal. The amplifier then passes the signal on to the ADC (Analogue to Digital Converter), and also notifies the TDC (Time to Digital Converter) and trigger logic that an event has been detected. The ADC then determines a channel number based on the amplitude of the signal, since this value is proportional to its energy. The TDC determines the relative timing of each signal, and digitizes it for readout. Finally the trigger logic must then either accept or reject the event, and informs the ADC and TDC of its decision. The readout is only performed if the trigger logic accepts the event.

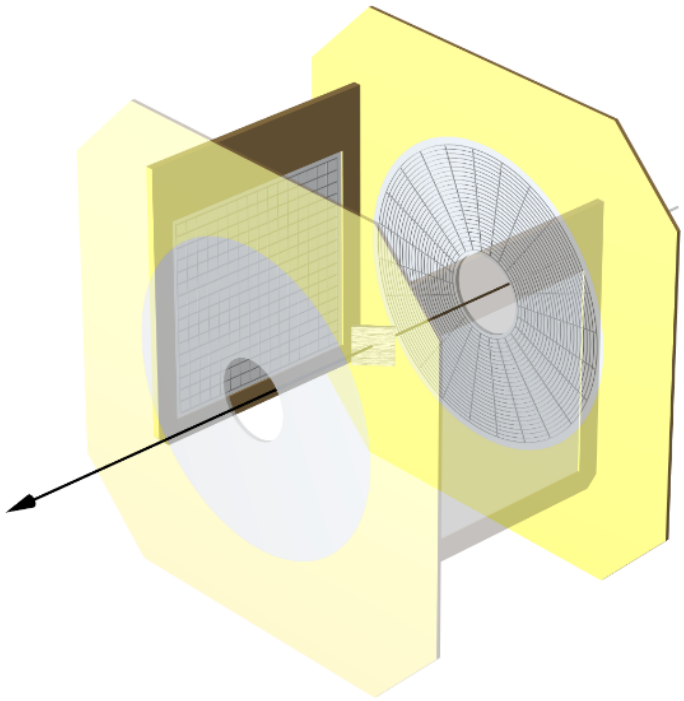

Figure 7: The experimental setup. Note the large solid angle covered by the detectors. The figure is reproduced from Kuhlwein [9].

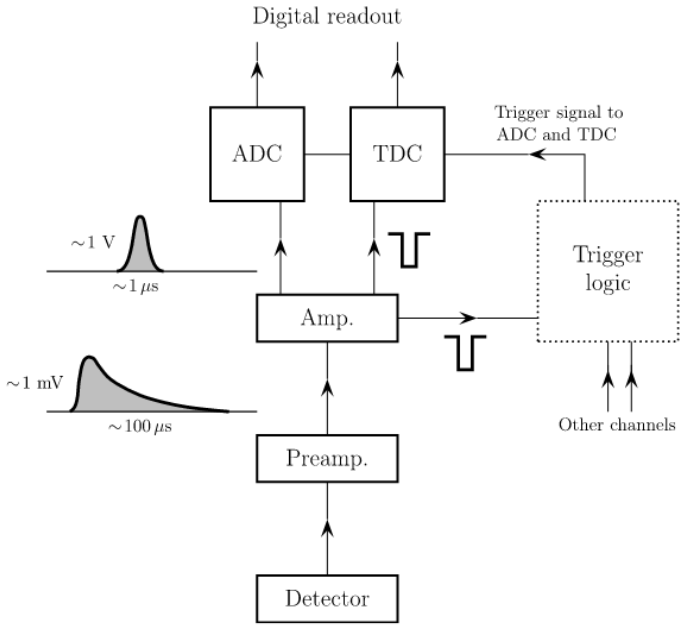

Figure 8: An overview of the main components of the data acquisition system. The figure is reproduced from Kirsebom [30].

4 Data reduction

Having gathered the raw data as explained in the previous section, it is now time to shape it into a form better suited for the subsequent analysis. Since this step is common to most types of experiments, a set of powerful tools have been developed to streamline the process.

4.1 Tools

`ROOT` [32] is an object-oriented C++ framework created at CERN in 1994. It was designed to be a replacement of the then-used `FORTRAN` library, which was quickly approaching its limits with the pure quantity of data being generated at the facility. Due to these roots, `ROOT` was originally designed to handle the high-energy physics data being generated at the facility in an efficient manner. In the many years since its conception, it has grown into a true stand-alone package capable of handling most types of data analysis.

`ROOT` contains a vast quantity of methods and classes for most conceivable types of analysis. The basic storage type relevant for this work is the `TTree` class, consisting of a number of named branches. Each branch corresponds to some variable of an event, such as the multiplicity or alpha energies. These trees can then be directly written to disk, which is the approach used by `AUSAlib` to store its data.

Another important type is the `RDataFrame` class, which in this context can be thought of as a wrapper around the `TTree`. It is then able to perform efficient and parallel operations on the underlying `TTree` structure through a simple interface. They are somewhat limited in their capabilities, however, and thus have mostly been used for generating plots.

`AUSAlib` (*Aarhus University Subatomic library*) [33] is another C++ framework built on top of `ROOT` developed here at Aarhus. Since the experimental setups are typically similar between different experiments, it would mean a rather large overlap in analysis code. Thus a common framework was created, intended primarily as a transformation tool from raw data to readily analyzable data. Since this process typically involves many distinct steps, `AUSAlib` consists of multiple individual modules, each handling one aspect of the transformation. As is common in such frameworks, it eventually grew beyond its intended use, and now also includes a simulation library called `simX`. The basic idea with this custom simulator is to account for the detection system in Monte Carlo simulations, such as to allow a direct comparison

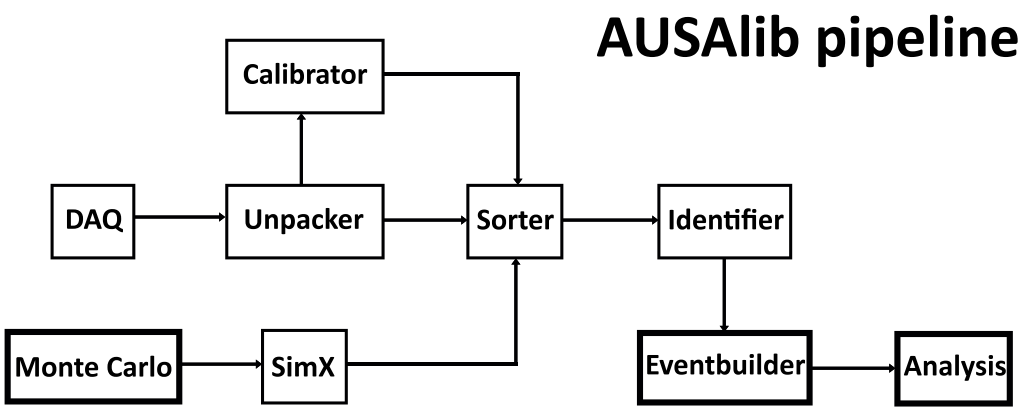

Figure 9: The `AUSAlib` pipeline. Boxes with thick lines must be either partially or fully implemented by the user.

with the experimental data.

The remainder of this section is devoted to introducing these individual modules. The next section discusses the practical application of them. For a brief overview of the whole library, see figure 9.

4.1.1 Unpacker

The first module converts the raw data from the acquisition system to a `ROOT` `TTree` format. This is done by utilizing the third-party unpacking program `ucesb` [34]. The setup-files for this program defines the general `TTree` branch structure which will be used throughout the rest of this project. Some of these branches will become relevant later, and so a brief introduction to them is in order. Associated with each event are the two vectors `FT` and `BT`, which are the `TDC` (time) values for the front and backside, respectively. They are vectors since they are particle properties, which each event may contain several of. Similarly `FE` and `BE` are the `ADC` (energy) values associated with them.

4.1.2 Calibrator

At this point, the energies and detection times are still stored in the form of channel numbers. Before they can be used in an analysis, they must be converted to a more meaningful form. The `Calibrator` is designed to handle one of these issues by converting the `ADC` channel number into an actual energy. To perform such a calibration, it is assumed that the channel num-

bers are linearly related to the energies. By then measuring a known source, its expected spectrum can be compared with the measured, thus uniquely determining the variables of the linear relationship.

When supplied with some input calibration data, the tool uses a peak-finding algorithm to roughly identify where the peaks are located. To obtain better estimates for the peak locations, this is followed by a multi-Gaussian fit. The distribution of peaks can then be compared with the expected energies, thus obtaining a list of (channel, energy) pairs. The final calibration is then found by simply fitting all of these pairs.

There is a further complication that must be taken care of, however. As mentioned in the previous section, all of the detectors have a small aluminum dead layer. All particles passing through thus loses some energy depending on the stopping power of the material. Furthermore, this energy loss is heavily dependent on the effective thickness of the dead layer Δx_{eff}, which again depends on the angle of incidence, θ. A simple geometric exercise gives the relationship between the effective and actual thickness as $\Delta x_{eff} = \Delta x / \cos\theta$, such that the net effect can be described as

$$E' = E - \frac{dE}{dx}\frac{\Delta x}{\cos\theta} \tag{28}$$

where E is the original energy of the particle, dE/dx the stopping power of the material, and Δx the actual thickness of the dead layer. The stopping power is calculated with `SRIM` [35].

All of this is handled by the `Calibrator`. As input it takes the unpacked input of a measurement of a single source, along with a file specifying the locations of the expected peaks. From this the tool corrects for the energy loss and establishes a linear relationship between channel numbers and energies. The result of this is then written to disk in a separate calibration file, which is passed as an argument to some of the other modules. Note that the tool does not modify the input data, meaning that the dead layer energy loss is still unaccounted for. Instead the `Calibrator` corrects the expected energy spectrum, meaning that the resulting calibration is still valid. Correcting for the effect in the data itself will be left to the `Identifier` module, which will be introduced later.

4.1.3 Sorter

The purpose of the `Sorter` is to generate new `ROOT` files based on the unpacked data. During this process, various operations can be applied on the

data, such as applying a previously determined energy calibration. Another important operation is matching and combining events from the front and back sides of each detector. If only a single hit is detected on each side, this is trivial. If there are multiple, a greedy matching algorithm sequentially picks the pair of hits with the lowest energy difference.

After this event matching has been performed, the hits on the individual sides of each detector are merged into a single combined event. This means that we can now effectively think of each event as consisting of multiple *particle* hits. Thus it is now possible for us to associate physical properties with each particle, such as the polar or azimuthal angle. Since we have still not performed any filtering, each event still consists of an arbitrary number of particle hits. To perform such a filtering, we need the next module.

4.1.4 Identifier

The `Identifier` is, as its name suggests, meant as a tool for identifying the participating particles. As mentioned previously, it is also responsible for carrying out the energy loss corrections, not only due to the dead layers of the detectors, but also due to passage through the target.

The standard approach to identify particles is to place a second detector behind the thin DSSD. The particles then lose some energy depending on the stopping power of the DSSD, which is in general particle-specific. Their remaining energy is picked up by the second detector, such that it is easy to deduce how much energy they lost in transit. Another approach is to look at the energy deposited in the DSSD, which may be too large to come from a lighter particle, which can thus be excluded.

No secondary detector was used in this setup, and the second approach cannot differentiate between protons and α-particles. Thus this functionality could not be used, and the `Identifier` was used solely for its energy loss corrections.

4.1.5 EventBuilder

The final module of the standard `AUSAlib` pipeline is the `EventBuilder`. The purpose of it is to remove any dependency on the experimental setup from the data, leaving only the physical events. To do this, each reaction is reconstructed, and the user must decide on some criteria to either accept or reject a given reaction. As an example, one can require that at least two

particles participated in the reaction.

The module also allows the user to define new properties, such as the four-momenta of each particle, which can then be used for further analysis. The module is not meant for aggregate analysis of the data, but only of each individual decay event. Since this is quite a restriction, the tool is used mainly as a filter. Any further analysis can then be written as standalone C++ scripts, which can be found in appendix C.

4.1.6 simX

When comparing the measured data with a theoretical model, two distinct steps must be simulated: the actual physical process, and its interaction with the experimental setup. `simX` handles both of these. It can also be configured to take the first step as input, and only simulate their interaction with the detection system, which allows users to generate their Monte Carlo data in any way they like.

The simulation is based on the three-body decay extension of R-matrix theory as mentioned in section 2.2.5. By neglecting Bose symmetry, one can derive the following equation for the decay amplitude [36]

$$|f|^2 \propto \frac{\Gamma_1\Gamma_2}{E_{2-3} - E_0 - \gamma_2^2[S_{l'}(E_{2-3}) - S_{l'}(E_0)]^2 + \Gamma_2^2/4}$$

which is the foundation of this simulation tool. In this equation, Γ_1 and Γ_2 are the widths for each step of the decay, related to γ_1 and γ_2 through (13). E_0 is then the formal energy of the ^{8}Be resonance. To improve the accuracy of the tool, an angular correlation function can also be supplied. These were calculated with my own tool, to be introduced later. The most relevant correlation functions can be seen on table 1.

The output of `simX` is an unpacked `ROOT` file with a structure identical to the output of the `Unpacker`. This means that after a simulation is performed, the data can be subjected to the exact same operations as the experimentally measured data, right up to the analysis itself.

State	$W(\beta)$
0^+, $l = 2$	$\frac{45}{4}\cos^4\beta$
2^-, $l = 1$	$\frac{3}{2}\sin^2\beta$
2^-, $l = 3$	$-\frac{45}{8}\cos^4\beta + \frac{21}{4}\cos^2\beta + \frac{3}{8}$
3^-, $l = 1$	$\frac{3}{7}\cos^2\beta + \frac{6}{7}$
3^-, $l = 3$	$\frac{15}{4}\cos^4\beta - 4\cos^2\beta + \frac{19}{12}$

Table 1: The relevant correlation functions calculated with my own tool.

4.1.7 sim3a

This final module is not officially part of `AUSAlib`, but is rather a small tool written by a previous student. The tool performs Monte Carlo simulations of the specific reaction $^{12}\mathrm{C} \longrightarrow {}^{8}\mathrm{Be} + \alpha$ based on the following R-matrix expression, first proposed in [37]:

$$f_{1,23} \propto \sum_{m_b} (l m_a - m_b j_b m_b | j_a m_a) Y_l^{m_a - m_b}(\Theta_1, \Phi_1) Y_{l'}^{m_b}(\theta_2, \varphi_2) \times \frac{\sqrt{\Gamma_1 \Gamma_2 / \sqrt{E_1 E_{2-3}}} e^{i(\delta_{l'} - \phi_{l'})}}{E_0 - \gamma_2^2 [S_{l'}(E_{2-3}) - S_{l'}(E_0)] - E_{2-3} - \frac{i}{2}\Gamma_2} \tag{29}$$

Here (Ω_1, Θ_1) and (ω_2, φ_2) are the emission directions for the primary and secondary particles in the center-of-mass frames of $^{12}\mathrm{C}$ and $^{8}\mathrm{Be}$, respectively. j_a and j_b are then the spins of these two states, and $\delta_{l'} - \phi_{l'}$ the Coulomb minus hard sphere phase shift, as presented in section 2.2.4. As the indices on $f_{1,23}$ implies, this equation defines a definite order of emission. Since we are dealing with three identical bosons, we need to symmetrize it as

$$f_l = f_{1,23} + f_{2,13} + f_{3,12}$$

which will then introduce interference effects in the simulation.

A trivial generalization of (29) is to allow for multiple orbital angular momentum values for the first α particle. When running in this mode, the tool outputs the decay amplitudes f_l and $f_{l'}$, from which the total decay amplitude can be calculated as

$$\begin{aligned} |f^2| &= \sum |\sqrt{k} f_l + \sqrt{1-k} e^{i\delta} f_{l'}|^2 \\ &= \sum \left[k|f_l|^2 + (1-k)|f_{l'}|^2 + 2\sqrt{k(1-k)} \big(\mathrm{Re}(f_l f_{l'}^*) \cos\delta + \mathrm{Im}(f_l f_{l'}^*) \sin\delta \big) \right] \end{aligned} \tag{30}$$

where l and l' are the two possible angular momentum values, and k is the mixing ratio of the two states. We have in this equation also introduced the phase δ, which is an additional relative phase difference between the two partial waves. The reasoning behind this is that the theoretical expression (30) paints a strictly sequential picture. This additional phase difference is then an attempt to allow for a possible divergence from this picture. Principally we would expect this additional parameter to vanish, but we will let the fitting algorithm be the judge of that.

The output of this program is a `ROOT` file which can simply be passed to `simX`, after which it can be pulled through the entire `AUSAlib` pipeline similarly to the experimental data.

4.2 Custom tools

Besides the tools contained in these public libraries, a few custom tools were developed specifically for this thesis. These will all be introduced here.

4.2.1 Dalitz fitter

Although we are working primarily with the 0^+ resonance which should allow only $l = 2$ transitions, we will eventually need a fitting tool which can fit the k and δ from the `sim3a` output. Besides this, we will also need to perform fits with 3, and sometimes even 4, different combinations of J and l, all of which will be handled by this Dalitz fitting script.

The name of the program, *Dalitz fitter*, signifies that it fits the Dalitz plots themselves, and not any of its projections. This choice is made due to a discussion of the pitfalls of fitting to projections presented in [9]. The basic idea of the program is to calculate the weights (30) for every iteration, and then use the modified maximum likelihood estimator introduced in section 2.5 to determine the optimal parameter values.

We now have an important decision to make: which minimization algorithm should we use? This choice is far more important than it may appear, since even with only 2 free parameters, most of the possible algorithms from `ROOT` actually failed to find the global minima. They were all tested on data from the 2^- state, based on which the best candidate appears to be the *Genetic* algorithm [38]. The basic idea is to randomly seed a group of individual "genomes" in the possible parameter space. A fitness function is then evaluated for every genome in each iteration, based on which they are either kept or discarded. A new generation of genomes is then generated based on the surviving population of the group. After a number of these cycles have occurred, the best genome is taken as the solution.

Since this algorithm randomly explores a large section of the parameter space, it is excellent for finding global minima. This same randomness also makes it extremely slow to converge towards a solution, and it was by far the slowest algorithm out of the ones offered by `ROOT` - each fit takes more than an hour to perform. These features are a boon for us, since it gives us more confidence in the accuracy of its results.

With the choice of algorithm made, we immediately encounter another problem: it does not support error estimates. To solve this issue, and simulta-

Fit parameter	Input: $\{J^{\pi}_{1,\,l}, J^{\pi}_{1,\,l'}\}$	Input: $\{J^{\pi_1}_{1,\,l_1}, J^{\pi_1}_{1,\,l'_1}\}, \{J^{\pi_2}_{2,\,l_2}\}$	Input: $\{J^{\pi_1}_{1,\,l_1}, J^{\pi_1}_{1,\,l'_1}\}, \{J^{\pi_2}_{2,\,l_2}, J^{\pi_2}_{2,\,l'_2}\}$
k_1	x	x	x
δ_1	x	x	x
c		x	x
k_2			x
δ_2			x

Table 2: Overview of the possible inputs to the Dalitz fitting tool. An input file is depicted by a pair of curly braces. The parameters k_1 and δ_1 describes the ratio and relative phase within the first `sim3a` input file, c describes the ratio of the first input file to the second, and k_2 and δ_2 describes the ratio and relative phase within the second `sim3a` input file.

neously ensure that the errors are accurate, i.e. follows the description from section 2.5, we can use the `MINOS` tool from `ROOT` [39]. When given a good estimate of the parameters, this tool determines the 1-σ errors by finding the set of parameters $\boldsymbol{\theta}'$ where $\ln \mathcal{L}(\boldsymbol{\theta}') - \ln \mathcal{L}_{max} = 1/2$.

Finally, a few words on how the tool handles simultaneously fitting multiple simulations. Any single or pair of `sim3a` simulations can be fitted, but any interference beyond that provided by the simulation tool is neglected. As an example, if we fit the simulated pair $\{2^-_1, 2^-_3\}$ and $\{3^-_1, 3^-_3\}$, the simulation tool accounts for interference within each pair. The fitting tool then creates two individual Dalitz plots, and adds them based on the ratio fitting parameter, thus neglecting any additional interference between the states. See table 2 for an overview of its functionalities.

4.2.2 Width converter

We will later have need of comparing simulations from `simX` and `sim3a` for a variety of different widths. Since the first uses the total width Γ and the second the reduced width amplitude γ, we will need to establish a relationship between the two.

We already have this relationship from equation (13), with only the interaction radius a_c as a free variable. Since this radius obviously depends on the strength of the Coulomb force, it will in general depend on the interacting nuclei. A popular choice for its value is to use the nuclear radii

$$a_c = r_0(A_1^{1/3} + A_2^{1/3}) \qquad\qquad r_0 \approx 1.4\,\text{fm}$$

which we will also do here, with $r_0 = 1.461\,\text{fm}$ determined by roughly matching the widths $\Gamma(^8\text{Be}^*)$ from [15] with $\gamma(^8\text{Be}^*)$ from [40].

The tool is implemented in Python due to its extensive library support. Thus the regular and irregular Coulomb functions can easily be calculated by using the mpmath library [41].

4.2.3 Correlation functions

This final tool simply calculates the correlation function $W(\beta)$ for any given input $\{j_1, j_2, j, l_1, l_2\}$ based on the theory from section 2.4. It was also used to generate the functions shown on the figures in that section.

For the same reasons as the width converter tool, this was also implemented in Python. Thus the Clebsch-Gordan and Racah symbols could easily be calculated with the SymPy library [42], which also provides the Legendre polynomials.

4.3 Data reduction

Here we will briefly discuss how these tools were used practically. The first step of the data reduction is to convert it to a format `ROOT` recognizes. This is done with the `Unpacker` tool, which converts the raw input to a `ROOT TTree`. After this step, the calibration files can be fed to the `Calibrator`, while the other files are passed to the `Sorter`.

A composite α-source consisting of the three isotopes ^{148}Gd, ^{239}Pu, and ^{244}Cm were placed in the target position, and rotated to face each detector in turn. Thus four separate sets of calibration data were generated, which could then be used as input for the `Calibrator`. The energies of each individual α-source is listed in table 3. However, due to some major issues which will be discussed in the next section, the calibration data for the 0^+ measurement could not be used. It was instead decided to reuse an older calibration from an earlier measurement of the 2^- resonance, which used the same setup.

Isotope	E_α [keV]
^{148}Gd	3182.690(24)
^{239}Pu	5105.5(8)
	5144.3(8)
	5156.59(14)
^{244}Cm	5762.64(3)
	5804.77(5)

Table 3: The decay energies of the composite target used for the calibration. They are taken from the NNDC [15].

After the energy calibration, the events from the front and backside of each detector is matched with the `Sorter` tool, effectively turning the list of detector hits into a list of detected particles. The `Identifier` is then used to correct for the energy loss due to passage through both the target and the dead layer of the detectors. After this, the data is finally passed to the `EventBuilder`, which deals with individual events.

The `EventBuilder` is the first tool which requires us to write our own code. The idea with this tool is that we can now specify all of the basic properties of each event that we will need in the actual analysis. It is also an excellent opportunity to perform some filtering based on these properties. The most noteworthy operations performed here are

- Multiplicity filtering: The data is separated into two halves depending on their multiplicity. For events where only two particles were detected, the third is reconstructed. After this stage, multiplicity 2 and 3 data are then treated individually. Note that each event may very well contain protons, which will be filtered by imposing a few different cuts.
- $\boldsymbol{p}_i$ definition: The individual momentum vectors for each particle is determined. We can then use these to calculate all angles that may be relevant in the analysis, such as the correlation angle β from (21). By also calculating and defining the total momentum p_t, we can then require that it not be too large.
- ΔE calculation: We calculate the "departure" from energy conservation for each event by subtracting the total α energy from the beam energy in the center-of-mass frame. Ideally this value would be 0 for all events (which it automatically is for the multiplicity 2 data), but since we are dealing with experimental data, the best we can do is require that it is at least close to 0.

Since we do not know the optimal cutoff values for the momentum and energy cuts, they cannot be performed here. That will instead be delegated to the first step of the analysis, which we are finally ready for.

5 Analysis

After having passed through the entire `AUSAlib` pipeline, the data is finally ready for the actual analysis. Before we perform any further calculations with the data, we first need to impose some cuts on it. The reasoning behind this is two-fold: one, to weed out any proton detections, and two, to ensure that any multi-coincidence α particle hits actually originate from the same decay event.

In total we would like to perform three cuts: one on the `TDC` values, another on the energy, and a final one on the momentum. Unless stated otherwise, all figures from this section are made with only multiplicity 3 data. We will also often use the notation J_l^π to specify specific transitions, where J is the angular momentum carried by the ^{12}C nucleus, π its parity, and l the angular momentum carried by the primary α particle.

All figures from this section were generated by our own C++ scripts, which can be found in appendix C.

5.1 TDC cut

The general idea with this type of cut is that a given α-particle should hit the front and backside of a detector within some small time interval. If this interval is too large, the two hits are probably not from the same particle, and the event should be discarded.

It turns out that this cut is not that simple to perform, however. There are two issues with the `TDC` values which must first be addressed. The first is a matter of alignment: the `TDC` values for the different strips are not necessarily aligned with each other. The second is a major issue which was discovered with the data for only the 0^+ measurement. We must first deal with the latter.

5.1.1 Repairing the data

To see the problem, look at figure 10. The figure contains all measured `TDC` values by the detectors (x-axis), both for the front and backside (y-axis). Only the backside of the S3 detectors were hooked up to the `TDC` converter, hence why the two bottom-left panels are empty. Two problems are clearly visible in this figure: one, we have too many peaks, and two, some of the

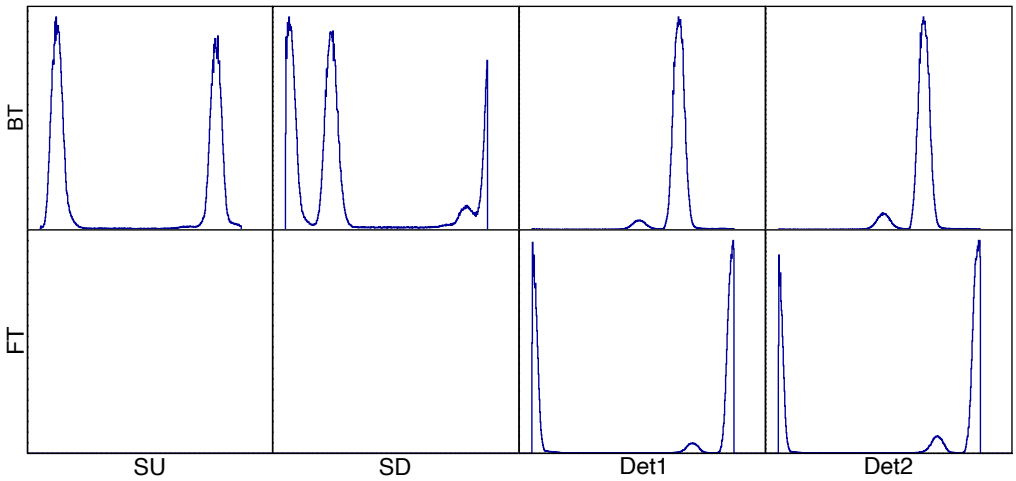

Figure 10: The issue with the TDC values. The values on the y-axis are the TDC values for the front (FT) and backside (BT). The x-axis labels the four detectors used for the experiment. Note specifically the major difference between BT and FT for Det1 and Det2; the FT peaks appear to be broken.

peaks appear to be broken in half. We will focus on the latter problem first.

Such a clean split down the middle of a peak, with its two halves appearing at the very edges of the plot, looks like a classic overflow problem, and indeed, it probably is. The right half of every broken peak stops at exactly $2^{16} = 65536$, which is coincidentally the same number of bits used for the TDC data word size. This clearly indicates that the problem is due to a simple overflow. However, things are not that simple: the left half of every broken peak starts at exactly 65126; i.e. the peaks are only shifted by 410, and does not overflow back to 0, as we would expect. Upon a closer examination of all data sets, it appears as if this range, $\{65126, 65536\}$ contains the *only* possible values for the TDC besides 0. Why this is the case is unclear, but since we are only interested in the *differences* between TDC values, we can choose to ignore the cause and simply fix the data.

Figure 11 shows the data after it has been corrected. This reveals another piece of the puzzle: the two halves of the peaks do not match up exactly. It is, however, a very close match, and so, once again, we have chosen to simply accept the data as it is.

With the second problem fixed, we now turn our attention to the first: we still have multiple significant peaks in essentially all our panels. The S3 de-

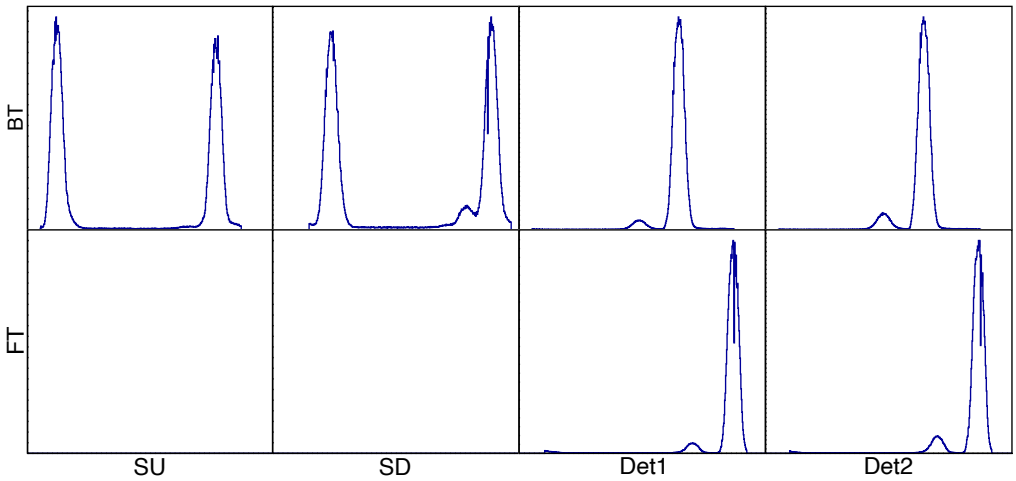

Figure 11: The corrected TDC values. The issue seen on figure 10 has now been corrected.

tectors especially are problematic. To understand why this is the case, we must first discuss some of the finer details of the detectors.

A detector A can be activated in two ways. The first case is when A itself detects a hit, after which it will immediately send a signal to the TDC converter. The second case is when another detector B is hit, and sends an activation signal to A. Due to the additional length of wiring the signal must pass through from B to A, the second case will in general be delayed compared to the first. Since the length of wiring may be different for signals from each detector $\{B, C, D, ...\}$, this may result in a unique peak for each. I will refer to these two cases as primary and secondary activations, respectively.

These two types of activations are exactly what we see on figure 11, which we can realize by separating the data into different sets depending on the multiplicity. For multiplicity 1 data (we are temporarily working with the data before these events were discarded), only primary activations can occur. For higher multiplicities, both primary and secondary activations should be present, with an increasing number of secondary compared to primary as the multiplicity increases. This is exactly what we see on figure 12, showing only the BT peaks. The FT peaks for the W1's acts identically. This interpretation also explains why the secondary peaks for the S3 detectors are relatively larger than those for the W1s: since the upstream SU only detects backscattered particles, and the downstream SD is heavily downscaled, we would expect the W1s to be mainly primary activated, which is exactly what we see.

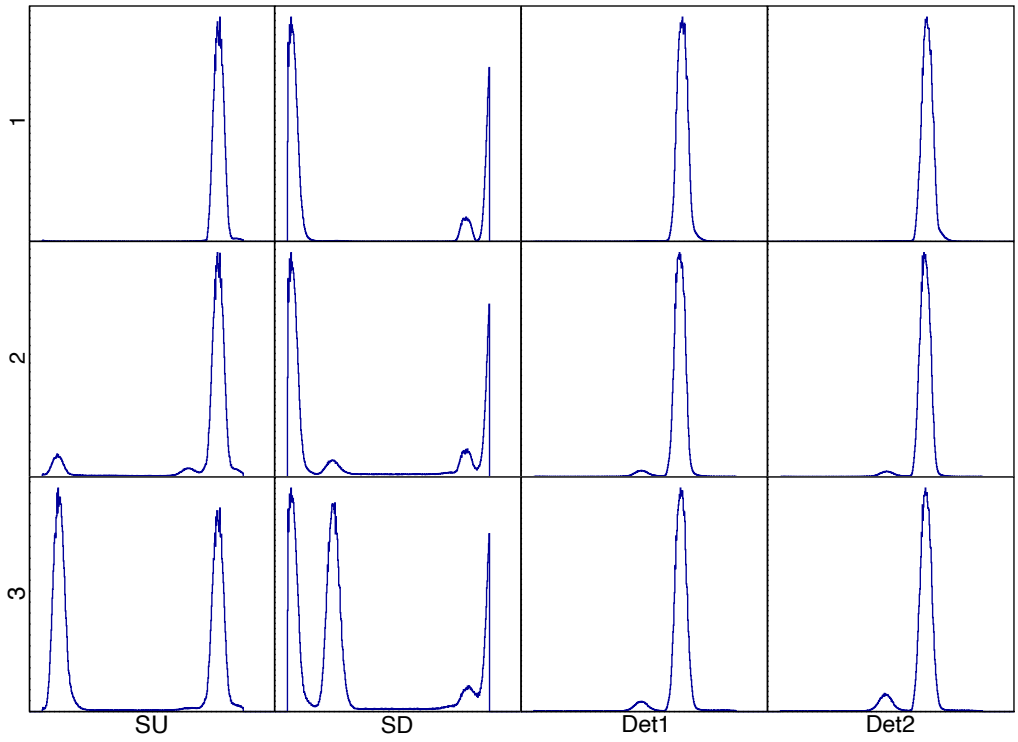

Figure 12: The second issue with the data. The y-labels denotes the multiplicity, while the x-labels denotes the detector. The multiple peaks are due to primary and secondary activations. See the text for a detailed discussion.

This explains all but a single extra peak, which can be seen on the second top panel from the left. Some further investigation reveals that this extra peaks consists almost entirely of low-energy events, as can be seen on figure 33 in the appendix. With the cause of every peak identified, we can now solve the problem by simply shifting all of them on top of each other, as can be seen for the `BT` peaks on figure 13.

5.1.2 Alignment

Now that we have fixed the issue with multiple peaks, it is time to look at the other problem of aligning the `TDC` values. For the remainder of this section, we are only interested in the *difference* in `FT` and `BT` values, which is problematic for the two S3 detectors since they only measure the latter. We can get around this problem by looking only at their multi-detector events, i.e. cases where the decay products were detected by at least two different detectors. As long as one of these two detectors are a W1, we can simply use

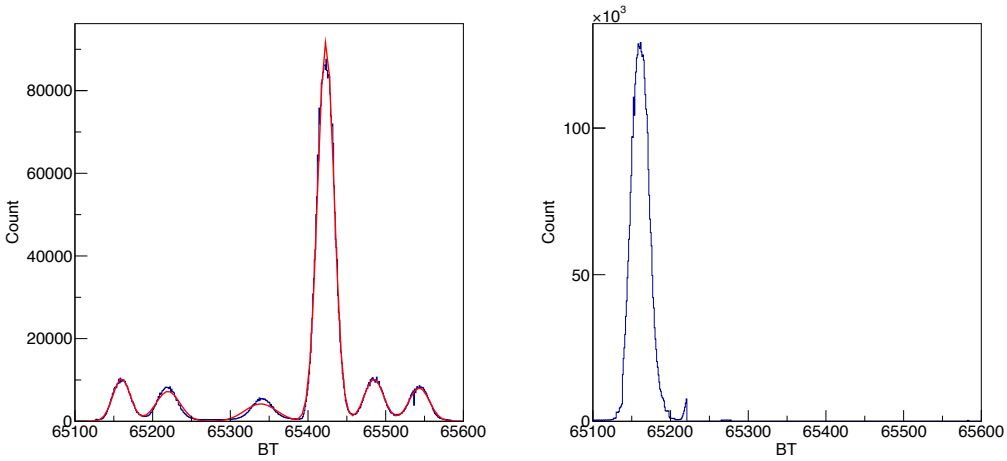

Figure 13: Shifting the multiple `BT` peaks on top of each other. The left panel shows the multi-Gaussian fit, which allows us to obtain the mean μ_i and standard deviation σ_i for each peak. The i'th peak is then moved by shifting all bins within $3\sigma_i$ by $\mu_i - \mu_0$, thus stacking it on top of the first peak. The result of this process can be seen on the right panel.

its `FT` value for the S3 as well. We can do this since this should simply be a constant offset from whatever the S3 would have measured by itself.

Now, to convince ourselves that it is actually necessary to align the `TDC` values, take a look at the two left panels of figure 14, which shows the difference in `FT` and `BT` values for the two detectors Det1 (top) and SU (bottom). As it is right now, it is impossible to fit the 1D projection with a Gaussian; hence the need for this alignment.

Before we start modifying the data, we need to discuss what we are actually allowed to do. When a strip sends a signal to the `TDC`, it must first travel through some length of wire, which takes some time t. Ideally these wires would all be the same length, or the `TDC` would be calibrated to account for the differences, which would automatically solve this alignment problem. Since this is not the case, our goal is to determine the difference in wire length, Δt. We do this by minimizing the equation

$$\sum_{\text{hits}} |(t_i + \Delta_i) - (t_j + \Delta_j)| \tag{31}$$

where $\{i, j\}$ run over the number of strips. We use the absolute difference instead of least squares since we expect outliers from random coincidences.

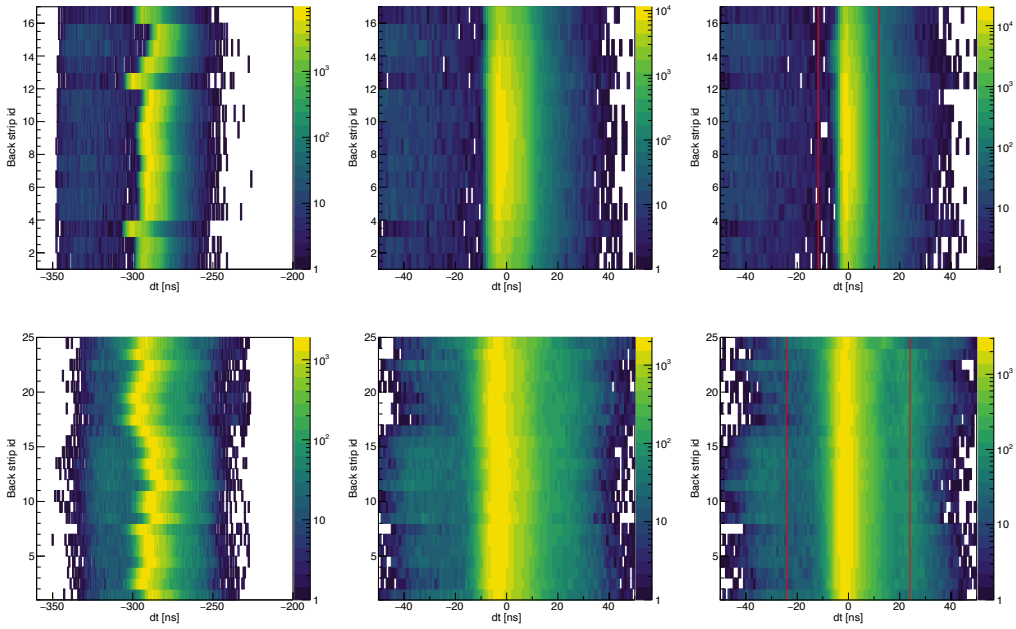

Figure 14: The three main steps of the `TDC` calibration. The top row shows the process for Det1, while the bottom row is for the SU. The left panels shows the raw data, neatly illustrating why it must be aligned. The middle panels shows the same data after each strip has been centered. The right panels shows the outcome of the minimization procedure, and also the results of the Gaussian fits. All events within the 3σ red lines will be kept.

The first step is to extract the mean dt for each strip, and use this to center them around 0 - this operation amounts to applying an offset to each Δt. As can be seen on the middle panels of figure 14, this already dramatically improves the alignment, but we can still do better. By now performing the minimization from (31), we arrive at the two right panels of the same figure. We can finally perform a Gaussian fit to this and only keep events within 3σ, which corresponds to the area enclosed by the red lines also shown on the two right panels.

With this cut applied, we are finally ready to move on to the energy and momentum cuts.

5.2 Energy & momentum cuts

To help guide our choice of cutoff values, an obvious first step would be to plot the energy against the momentum in a 2D histogram. This can be seen in figure 15, which shows the raw data in three cases: before any cuts (left),

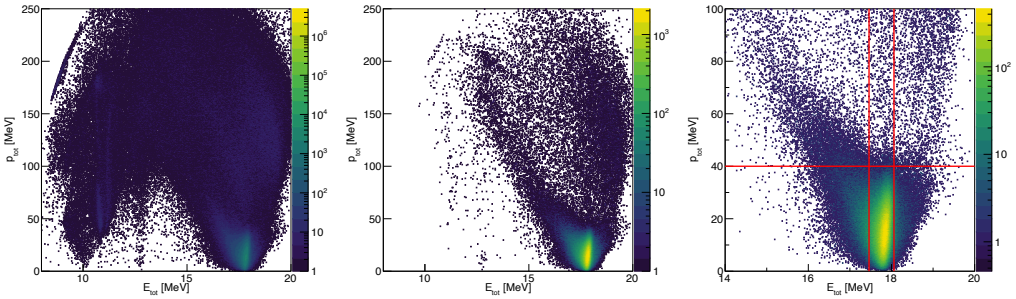

Figure 15: The effects of the three cuts. The left panel shows the raw data, without any cuts. The middle panel shows the same data after the `TDC` cut has been applied. The right panel is a zoomed-in version of the middle panel, where the vertical and horizontal lines illustrates the energy and momentum cut, respectively. Note the different column scale in each panel.

after the `TDC` cut (middle), and the energy/momentum cut (right). The cut-off values for energy and momentum were manually selected to preserve the central events around $E_{tot} = 17.76\,\text{MeV}$. With all our cuts imposed on the data, we can finally continue with the actual analysis.

5.3 Dalitz plots

The purpose of this thesis is to test the validity of the currently established models for the 0^+ state. Thus a nice opener to the analysis is to make a Dalitz plot of the data. This plot can be seen on the left panel of figure 16, which reveals that another cut is necessary. The figure shows that a large concentration of events are located in a band near $y \simeq 1$, where almost the entire energy of the first decay is given to the primary α particle. These events thus corresponds to decays through the ground state of ^{8}Be, i.e. through the α_0 channel. A simple way of getting rid of these α_0 events would be to impose a cut on the y-coordinate, which is shown in the middle panel of the same figure. We can do even better than that, however, if we look at the momentum vectors instead of the energies.

We can use the momentum vectors of each event to calculate E_{2-3} from (20), the distribution of which can be seen on figure 17. Here we clearly see the two peaks corresponding to the α_0 and α_1 channels, located at their expected energies - note the split in the x-axis. By now performing a simple Gaussian fit of the right peak and discarding any event outside 3σ, we can extract only the excited decay events, which can be seen on the right panel of the Dalitz

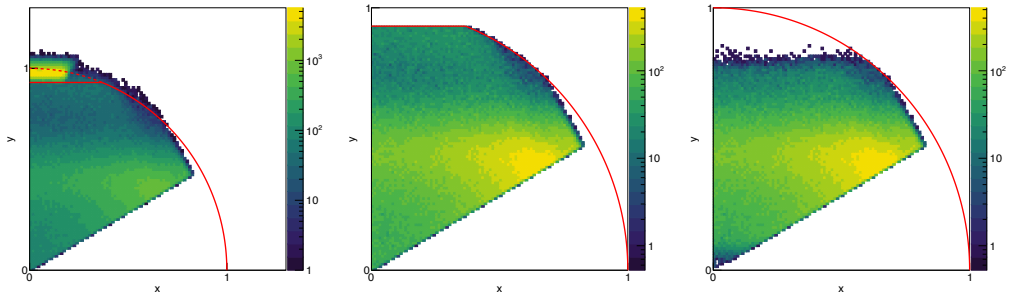

Figure 16: The cuts on the Dalitz plot. The left panel shows the data before any cuts, with the red lines signifying the cutoffs. The middle panel shows the same data after the simple y-coordinate cut. The right panel also shows the same data, but with a cut based on the E_{2-3} energies.

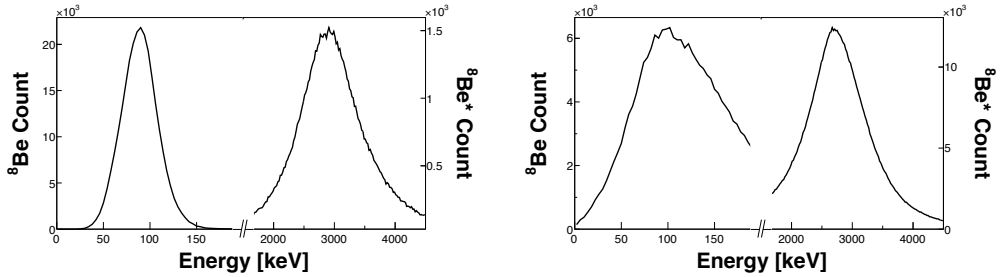

Figure 17: The E_{2-3} values from (20). The left panel shows the plots for our multiplicity three data, while the right shows it for the multiplicity two data. The left peak corresponds to ground state decays, while the right peak is for excited decays. Note the difference in both the x and y axes for the two peaks.

slice panels, figure 16. Although this method is even more aggressive than the simple y-coordinate cut, since it is based on the E_{2-3} energies, we can be confident that only irrelevant α_0 channel events are removed.

Since we have already fitted the E_{2-3} peaks, we can quickly count the number of events in each peak to estimate the branching ratio. The number of events within 3σ of each Gaussian peak can be found in table 4. A previous student estimated the detector efficiencies for the two decay channels, which are also listed in the same table. This was repeated for the 3^- data, which is the only other set where we already know the detector efficiencies. Due to a very broad α_1 peak, we have to restrict our counts to 2σ to avoid overlap - see figure 36 in the appendix. When comparing with the expected ratios which are also listed in the table, only the 3^- measurement agrees with the

expected value. The 0^+ measurement is not even close to our expectations. It is here worth keeping in mind that these expected values are taken directly from the NNDC [15], who cites Segel et al. [12] as their source. They mention that there are actually two solutions for its widths, where they argue that the higher value of $\Gamma_{\alpha_0}/\Gamma_{\alpha_1} = 0.403$ must be correct. However, in an earlier paper by Symons and Treacy [11], it is argued that the smaller solution of 0.209 is correct. If we instead compare to this smaller solution, our result is actually in fairly good agreement and is within 2σ. We will return to this discussion later.

Data	α_0 hits	α_0 eff.	α_1 hits	α_1 eff.	$\Gamma_{\alpha_0}/\Gamma_{\alpha_1}$	$\Gamma_{\alpha_0}/\Gamma_{\alpha_1}$ [15]
0^+	257 493	6.6(3)%	521 303	2.10(44)%	0.157(33)	~ 0.403
3^-	83 136	4.32(22)%	91 340	2.12(45)%	0.447(98)	~ 0.368

Table 4: The number of events within 3σ (2σ) of the E_{2-3} peaks for 0^+ (3^-). The expected ratios are taken from the NNDC [15].

We can also use the values from this table to set an upper limit on the contribution of 0^+ to the α_1 band. If we very generously assume that all of our α_0 hits originates from our 0^+ resonance, we can then use the branching ratio to estimate the expected number of α_1 hits. Scaling the number of α_0 hits by its efficiency, we get $257493/6.6 = 39014$. By then multiplying this number by the branching ratio, we would thus expect $39014 \cdot \Gamma_{\alpha_1}/\Gamma_{\alpha_0} = 39014 \cdot 1/0.403 = 96809$ α_1 hits from the 0^+ resonance. Compare this to the $521303/2.1 = 248239$ we have seen. This means that we would only expect the 0^+ resonance to make up $96809/248239 = 39\%$ of our hits. If we instead use Symons value, we can expect to see up to 79%, which is more sensible. Remember, however, that these numbers are based on the best-case scenario where *only* the 0^+ resonance contributes to the α_0 band.

Now that we have imposed all of the necessary cuts, we are ready to start the analysis of the plot itself. Although all of the kinematic information is already stored in a single slice, it is somewhat easier to see the structure in a standard Dalitz plot. We can reconstruct it by repeatedly mirroring the slice along one of its edges. By doing this, we obtain figure 18. The left panel shows the multiplicity three data, while the right panel shows the multiplicity two data. The general structure is clearly seen to be similar to an inverted equilateral triangle, with somewhat bent sides in the right panel. Although they both share this structure, there are also a series of important differences. Firstly, the three vertices do not extend all the way out to the edge in the left panel, while they do in the right. Secondly, the left panel has *zero* events

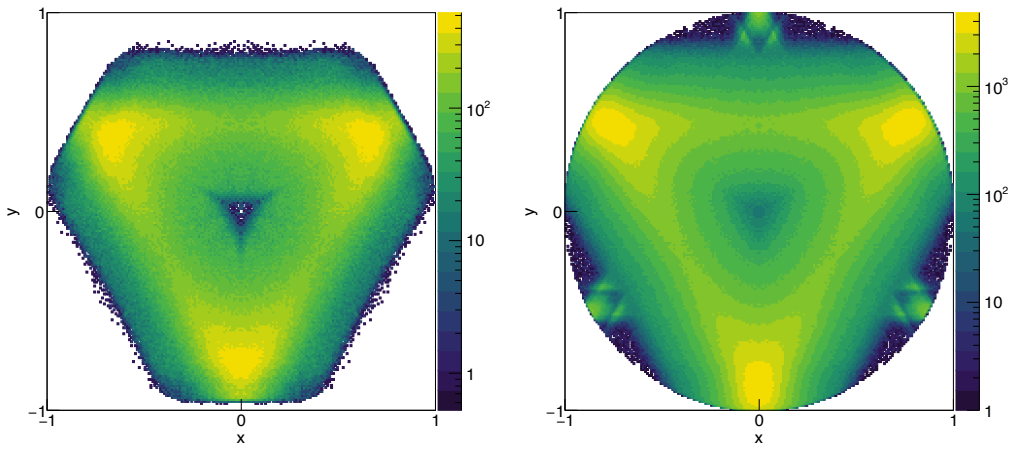

Figure 18: The Dalitz plots for the data. The left panel shows the plot for our multiplicity three data, while the right shows it for the multiplicity two data. Note the large difference in the column scale.

in its very center, while the right still has a few. Thirdly, we see some weird cone-shaped structures at the very top of the right panel. These cones are clearly unnatural, and probably originates from reconstructed events with random proton coincidences which has managed to survive our cuts. To see why this is the cause, the raw Dalitz plots without any cuts can be found in the appendix, figure 34. Here the cones can be seen to extend all the way outside the inscribed circular area, meaning they do not conserve energy - a very clear indicator that they contain protons.

Since the Dalitz plots are so different, it would be interesting to see how the phase space distribution changes between multiplicity 2 and 3 data. As was discussed in the theory, the entire allowed region of the Dalitz plot has a constant phase space volume. The easiest way to generate a sample of this volume is through a `sim3a` simulation, where each event must be weighted by equation (30). The simulated data is then put through `simX`, which simulates its interaction with the experimental setup. By then plotting the unweighted events after this step, we get the two panels in figure 19. Here the left (right) panel is the phase space for multiplicity 3 (2) data. There are some clear differences between these two, especially around the edges. Near the right edge, the left panel is suppressed, while the right panel is particularly dense. This makes good sense as this is the area where two of the particles are emitted in roughly the same direction, see figure 5. Since this edge coincides with a vertex in our data, it would explain why the plots looks so different in that

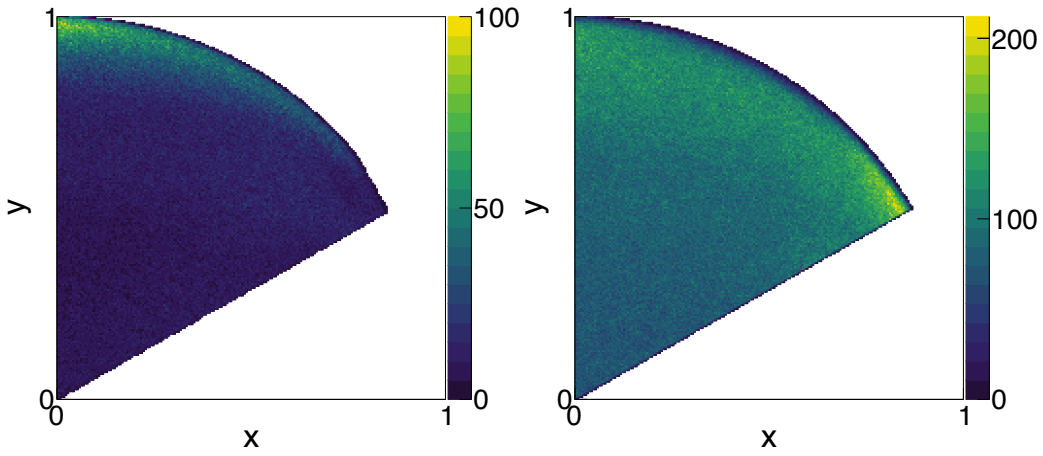

Figure 19: The phase space volumes generated by a `sim3a` simulation. The left (right) panel shows the multiplicity 3 (2) events.

area. The multiplicity 2 plot is particularly good at picking up events in the area, and thus the vertex extends all the way out to the edge. On the other hand, the multiplicity 3 data is particularly bad in that area, and thus the vertex is located further inside the borders. However, this cannot explain why the area appears to be cut completely in our multiplicity 3 Dalitz plot. Similarly the phase space plots does not give us any hints as to why the center and general curvature are different.

Our next goal is to figure out what we expected to see on our Dalitz plots. Although Zemach's analysis does not impose any constraints upon a 0^+ resonance, it is curious that the center appears to be suppressed. To get further than this, we will have to perform simulations of the decay. In section 4 we discussed two possible simulation tools, `simX` and `sim3a`, both based on R-matrix theory. Only the latter accounts for our three identical bosons and the interference between them, and it is thus our preferred choice.

The result of a `sim3a` simulation can be seen on the left panel of figure 20. Something is clearly very wrong here: it does not at all look like our data. More specifically, there is no evidence of an inverted equilateral triangle, and the center is not at all suppressed. As a quick check, another simulation was performed solely with `simX`, which results in the right panel of the same figure. While this is a far better match to our data, the edges around the vertices still look very different.

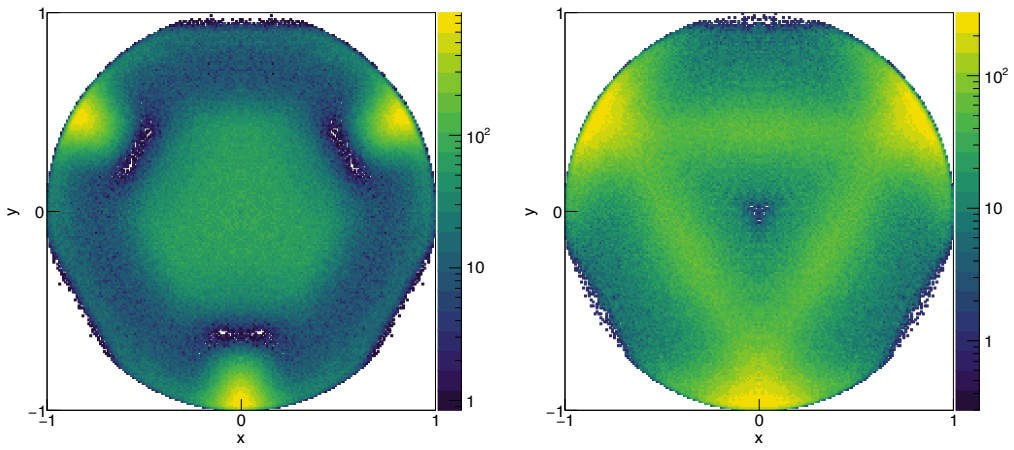

Figure 20: The Dalitz plots for the 0^+ simulations. The left panel shows the results of the `sim3a` simulation, while the right shows it for the `simX` simulation.

5.3.1 Checking the simulation tools

Since the simulations are so different from what we see in our data, it is worthwhile to verify that they actually work as expected. Since we also have data on the 2^- resonance which has been the subject of several papers (see e.g. [9]), it is an obvious target for checking the tools.

Using the custom Dalitz fitter introduced in section 4.2 to fit our multiplicity 3 2^- data with a `sim3a` simulation for both 2_1^- and 2_3^-, we get figure 21, which we can already at a glance tell is a far better match than the 0^+ resonance. The reason the simulation appears "grainy" is due to a low number of simulated events, which cannot be increased any further due to time constraints. The fit already takes an hour to perform, and, if we are optimistic, scales linearly with the number of events. Since we will need quite a few more of these fits later, the simulated number of events was limited to a million, from which about 20% survives all the cuts and contributes to the actual fit. Visually, this fit is excellent, but since it is rather hard to compare 2D histograms by eye, it is common to look at their projections instead. A popular choice are the polar projections, along with the center-of-mass energies. If we plot these, we get the three panels shown on figure 22. Here the black lines represents the data, while the orange represents the simulation. Although there are some deviations, especially for the radial projection ρ, this is overall a great fit to the data. For χ^2 and fitted values, see table 5.

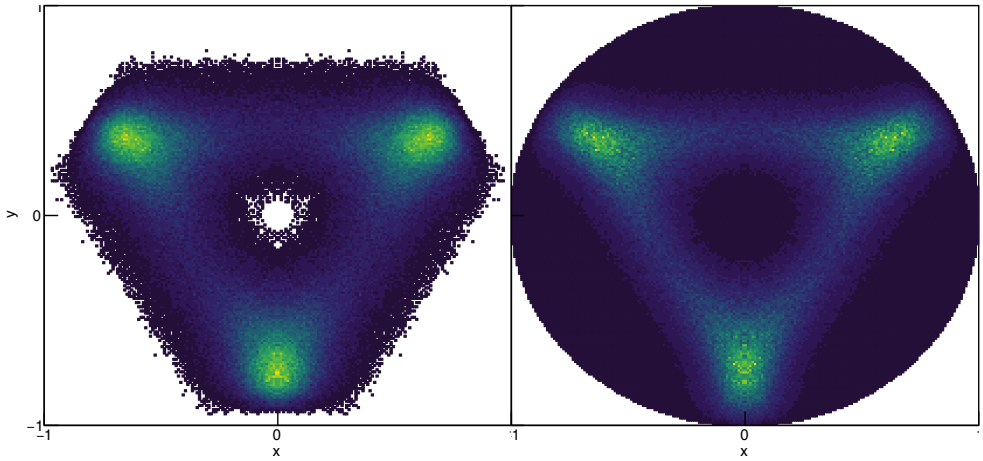

Figure 21: The Dalitz plots for the 2^- resonance. The left panel shows the original Dalitz plot, while the right shows a fit to the `sim3a` simulation.

As mentioned previously, this is the exact same 2^- data as that used in [9]. Although there are some differences in the techniques used to filter the data, the results are very similar, as can be seen in table 5.

	This paper	Kuhlwein [9]
k	19.8(5)%	20.5(2)%
δ $[2\pi]$	67.4(2)%	67.10(2)%
χ^2	13 453	14 028
dof	5347	∼5700

Table 5: The main differences in the analysis performed here and in [9]. Kuhlwein can do even better than this by also accounting for Coulomb interaction effects on the final states, a discussion we will return to later.

With an assurance that the simulations are not wrong, we can instead turn our attention to the R-matrix parameters they use. Kuhlwein found that for the 2^- data, the optimal values were generally not in agreement with prior research, and it is thus very likely that the same would apply to the 0^+ data. Thus it would be interesting to look at how our choice of parameters affects our Dalitz plots.

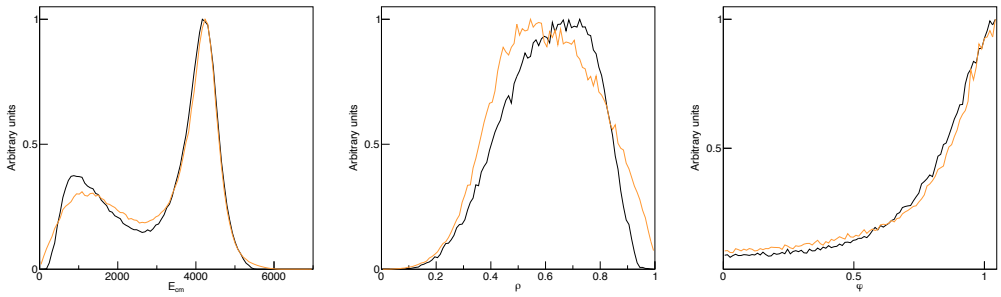

Figure 22: The projections of the two 2− Dalitz plots from figure 21. The black lines represents the data, while the orange lines are the simulation. The two lines match nicely in all of the projections.

5.3.2 Checking the reduced width amplitude

A solution to our problem could be that the reduced width amplitude used for the first excited state of ^{8}Be* is wrong. We have consistently been using the value $\gamma = 32.787\,\sqrt{\text{keV}}$ as found by [40]. While we examine the effects of changing this value, we can simultaneously use it as an additional check on our two simulation tools: as the width becomes smaller, interference effects becomes less relevant, and so the two simulations should converge towards each other for low γ.

As we discussed in section 2 of the theory, in a sequential three-body breakup, the angle between the primary and secondary particles are correlated. We also derived the correlation function $W(\beta)$ (24) for an arbitrary state. Combined with the equation for $\alpha = \pi - \beta$ (19), we can use this angle to compare the angular correlation implicit in the simulations with what we would expect for a 0^+ resonance. The angle α depends only on the Dalitz coordinates x and y, meaning we can easily extract it from a Dalitz plot by projecting down onto the x axis. Since it depends also on the y coordinate, we must limit the projection to a small area around an interesting area. With these simulations, that area is the main horizontal band, which can be seen on figure 23 for both `sim3a` and `simX`.

This figure consists of two separate plots: the top two rows shows the output of `sim3a`, while the bottom two shows `simX`. The reduced amplitude width γ used for each plot is used as the x label of the top panels, while the corresponding formal width Γ is used as the label for the bottom panels. This plot is mainly for illustrating the relationship between the Dalitz plots and the correlation angle. Since we will be analyzing these two parts separately,

figures 24 and 25 shows them individually.

Let us first focus on the structure of the Dalitz plots. When looking at figure 24, the effects of changing γ for the `sim3a` simulation becomes very apparent. As mentioned earlier, the value used for the previous Dalitz plot, figure 20, was $\gamma = 32.787\sqrt{\text{keV}}$, where only the three vertices and an abundance of events in the very center could be seen. We now see that both of these areas are the results of a large amount of interference between the connecting bands: starting from no interference in the top left panel, it gradually becomes more apparent until it is the only remaining feature for $\gamma = 40$. Similarly we also see an increasing amount of interference as the lines broaden on the `simX` panels, although no destructive interference can be seen there. Even when changing this width, none of the panels are a good match for our data. This would imply that the data may not be from a 0^+ at all, which we will explore later.

The other figure 25 shows the extracted correlation angle from each of the Dalitz plots of figure 24. The agreement between theory and simulation for `sim3a` is generally quite good, except at the points of maximum interference. `simX` is not quite as good, especially around the points of interference, and generally appears to be more smeared. The general shape is clearly seen in both figures, indicating that they work as expected. This also provides further evidence to the previous statement: the 0^+ correlation function predicts the "holes" we see on the simulated `sim3a` Dalitz plots, but which were not present in the data. This would then imply that the data does not follow the expected angular correlation distribution - we will take a closer look at this in the next section. Finally, the two tools does not really appear to be converging as γ decreases. It appears that this is mainly due to the `simX` simulations not being suppressed near the "holes", as they should. In an attempt to determine why, the tool was supplied with a variety of other correlation functions. The error appears to be consistent across them: in no cases could the input correlation be extracted from this type of plot.

As promised, the next step is to take a closer look at the distribution of the correlation angle of the data, since it does not appear to follow the expected distribution for a 0^+ resonance.

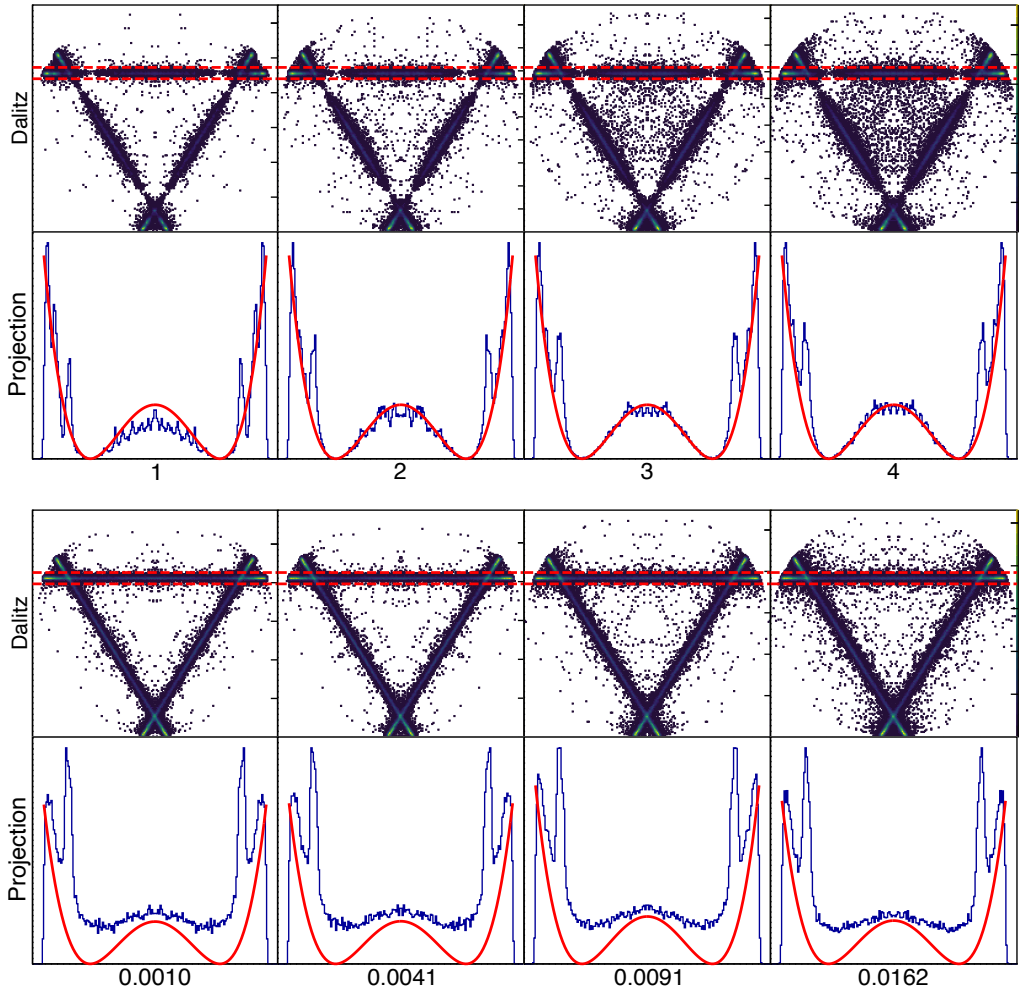

Figure 23: The top (bottom) figure shows the angular correlation distribution extracted from `sim3a` (`simX`). In each figure, the top row of panels shows the Dalitz plots along with the projected area around the main band. The bottom row of panels then shows the corresponding angular correlation distribution. The top figure uses the reduced width amplitude γ for its labels, while the bottom figures uses the corresponding total widths Γ.

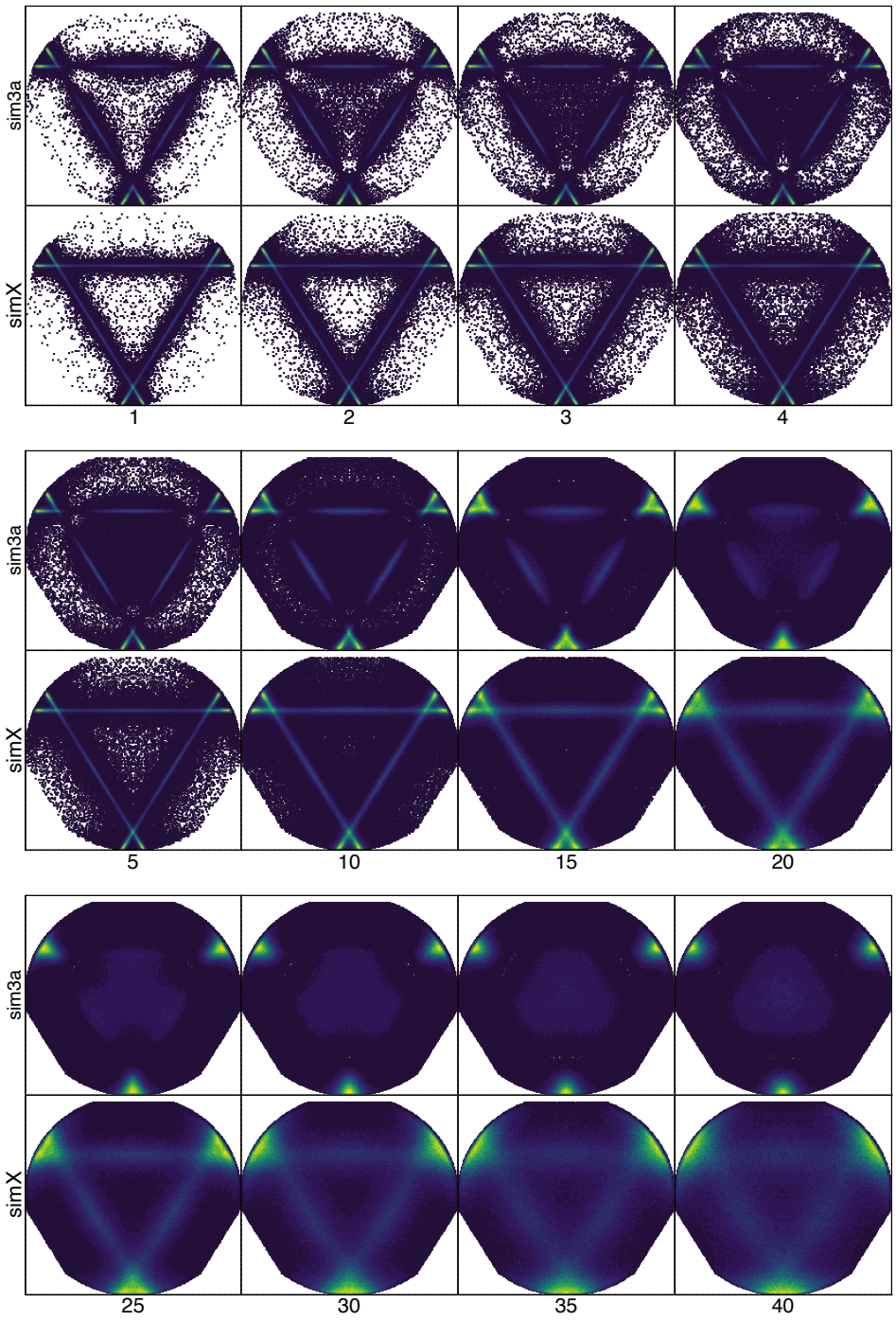

Figure 24: The dependency of the Dalitz plot of the 0^+ state on the widths. The labels for the x-axis are the reduced width amplitudes γ used for each column, where `simX` used the total width Γ corresponding to this value.

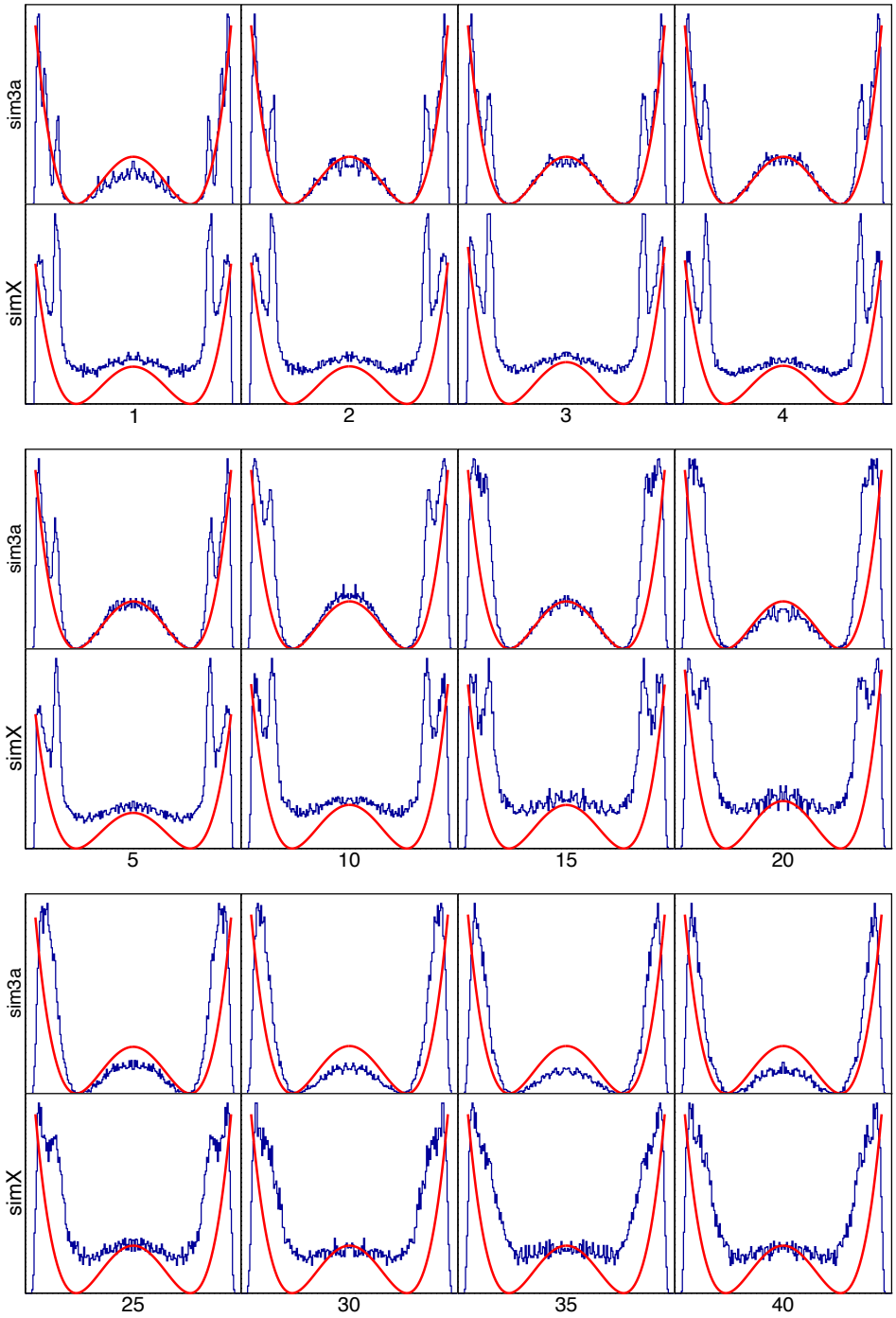

Figure 25: The angular correlation extracted from the Dalitz plots (see figure 24). Note how `sim3a` is almost perfectly described by the theory up to around $\gamma = 25$. At this stage interference effects becomes prevalent, which means that it is hard to estimate what the correct scaling for the theoretical expression is - the difference is most likely due to this. `simX` never quite seems to match the expected, which we in the text attributed to an implementation error in the tool itself.

5.3.3 Checking the angular correlations

We have two options for extracting the correlation angle from our data. The first option is to use the same method as in the previous section, where we extract the correlation angle α directly from the Dalitz plot. For the same reasons as was discussed there, a small area surrounding the main horizontal band was chosen, as can be seen on the top panels of figure 27. The projection itself is shown on both the bottom panels and on figure 26, where we will first focus on the latter.

On figure 26 the projection of the band along with all correlation functions up to and including the $J = 3$ states are shown. The idea with this figure is that we can visually check which correlation functions could potentially match our data. As we also discovered in the previous section, the shape of the 0^+ function is completely wrong, and could never possibly explain the data. Similarly we can rule out all of the states which peaks at $x = \pm 1$. We are then left with the options $\{1_2^+, 2_1^-, 2_3^-, 3_2^+\}$. Neither of these is a good match by themselves, so we need a linear combination of them. Both 2_1^- and 1_2^+ "undershoots" their prediction, and would need to be partnered with one or both of 2_3^- and 3_2^+, which "overshoots". Since 1_2^+ and 3_2^+ would both need to be partnered with another state, using those would imply our data is dominated by not only a single other state, but *two* others. Physically it would thus make better sense if we allow only a linear combination of the two 2^- transitions.

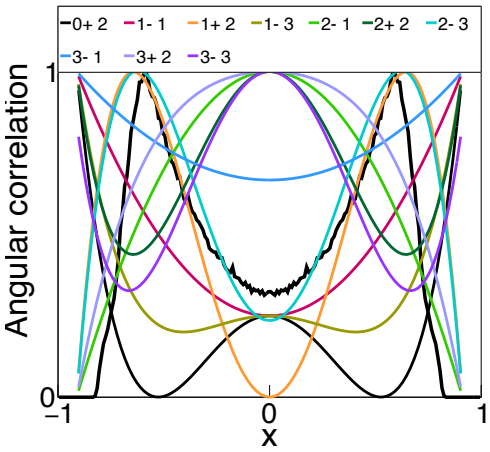

Figure 26: The correlation angle extracted from the data along with all relevant theoretical correlation functions. The 0^+ function is a terrible fit to the data.

Thus a fit with these two were made, which can be seen on the bottom panels of figure 27. An arbitrary scaling factor was also allowed as a free fitting variable, since a linear combination of the correlation functions is not necessarily normalized. We see that the fit is in remarkably good agreement with both our multiplicity 2 and 3 data, except at the points of maximum interference. Overall it is rather surprising that a simple fit of just two 2^- transitions is in

such good agreement with the data. After this first fit was made, a second fit which also allows for a 0_2^+ component was attempted. In both cases the ratio of this state was vanishingly low. The fit values can be seen in table 6.

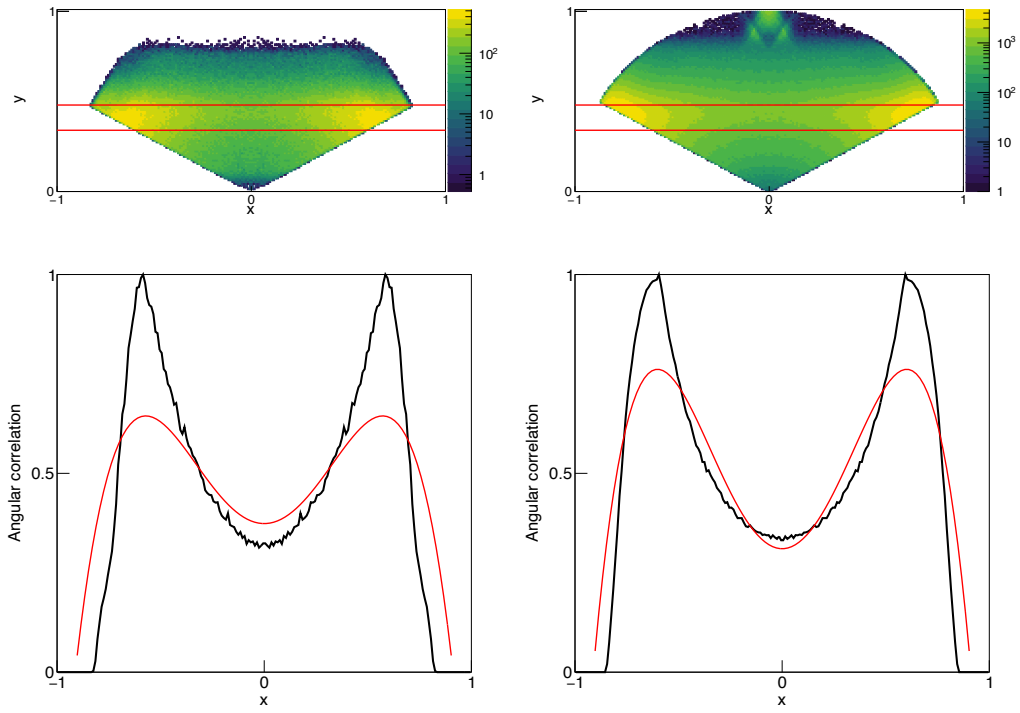

Figure 27: The correlation angle distribution. The top panel of the left (right) column shows the Dalitz slice, mirrored across the y-axis, for the multiplicity 2 (3) data. The area bounded by the solid red lines is projected down onto the x-axis, and the correlation angle α is calculated. The bottom panel shows a fit to this angular distribution, the result of which can be found in table 6.

Instead of hand-picking a specific area to project onto the x-axis, we can extract the angle β from the momentum vectors, as described by (21). These two angles are simply related by $\alpha = \pi - \beta$, as can be seen on figure 2. We can then repeat the analysis we made for the other angle, except we do not have to restrict ourselves to a small area, but can instead use all of the available data.

The results of doing this can be seen on figure 28, where the top panels shows the correlation angle for both α_0 and α_1 channel decays. The bottom panels then shows the actual fit, the results of which can be found in table 6. The multiplicity 3 fit roughly agrees with what we found through the α fit. The

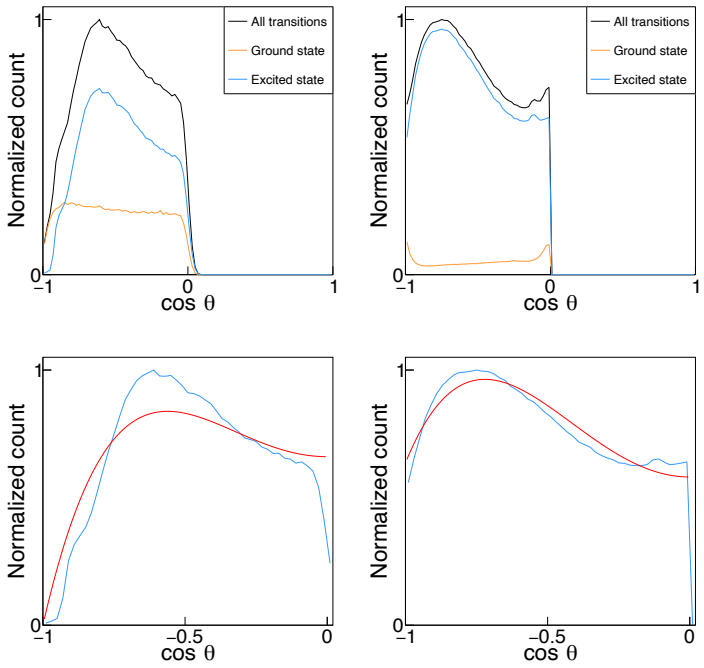

Figure 28: The correlation angle distribution calculated from momentum vectors. The top panel of the left (right) column shows the contribution of the α_0 (orange) and α_1 (blue) channels to the total distribution (black) for the multiplicity 2 (3) data. The bottom panel shows a fit to the α_1 distribution, the result of which can be found in table 6.

multiplicity 2 fit is far more interesting: it allows a substantial 0^+ component, and also appears to be the best fit we have seen so far. Graphically this makes sense since the 2^- functions both goes to zero at $x = -1$, which the 0^+ function must then make up for.

Correlation angle	Multiplicity	$k_{2_1^-}$	$k_{2_3^-}$	$k_{0_2^+}$
α	3	0.34(15)	0.66(15)	0(1e-13)
α	2	0.18(12)	0.82(12)	0(3e-11)
β	3	0.52(24)	0.48(24)	0(0.13)
β	2	0.14(22)	0.48(22)	0.38(20)

Table 6: The results of the fits seen on figures 27 and 28.

Physically, we would expect the $l = 1$ component to dominate due to the angular momentum barrier. Based on our results from table 6, they appear to be about equal for our multiplicity 3 fits, which may be due to the very large uncertainties associated with the fitting parameters. When we look at

these results, it is important to keep in mind that there is an inherent bias for the 2^- functions present. When the correlation angle α or β is close to some integer multiple of π, corresponding to bins near the edge of the Dalitz plot (see figure 5), two of the α-particles are emitted in the same direction. We would thus expect to find a relatively larger amount of multiplicity 2 events and a lower amount of multiplicity 3 events in that area, and indeed, that is what the densities of the phase-space plots from figure 19 tells us. In our correlation angle histograms, this would translate to an increase or decrease in the number of events at these angles. Since both of the 2^- angular correlation functions goes to 0 and 0^+ goes towards 1 in this area, it would mean that our multiplicity 2 fits would overestimate the 0^+ component, while our multiplicity 3 fits would underestimate it. This would nicely explain the difference between the two in table 6. Principally one could correct for this bias, especially since the phase-space densities are known, but this was not done here. The main takeaway from this fit is thus that the angular correlations are clearly dominated by a 2^- resonance, possibly with some small 0^+ component.

Although we found a 2^- assignation to be a good fit to the data, this should not be allowed since the resonance must have natural parity [11][12][14]. But with no other options to pursue, the best we can do is to continue following this trail and see where it leads. Thus the next step is to use the Dalitz fitting tool to try fitting our data with a a 2^- simulation.

5.4 Fitting the data

We will in this section perform a series of fits with the Dalitz fitting tool introduced in section 4.2. All results from this section can be found in table 7.

5.4.1 0^+

Based on the results of the previous section, it appears as if our data is dominated by a 2^- state, possibly with a small component of 0^+. With this knowledge, we can attempt to fit the data with such a state. By firing up the custom Dalitz fitter with the 0^+ data and a 2^- simulation, we get the result seen on the top two rows of figure 29.

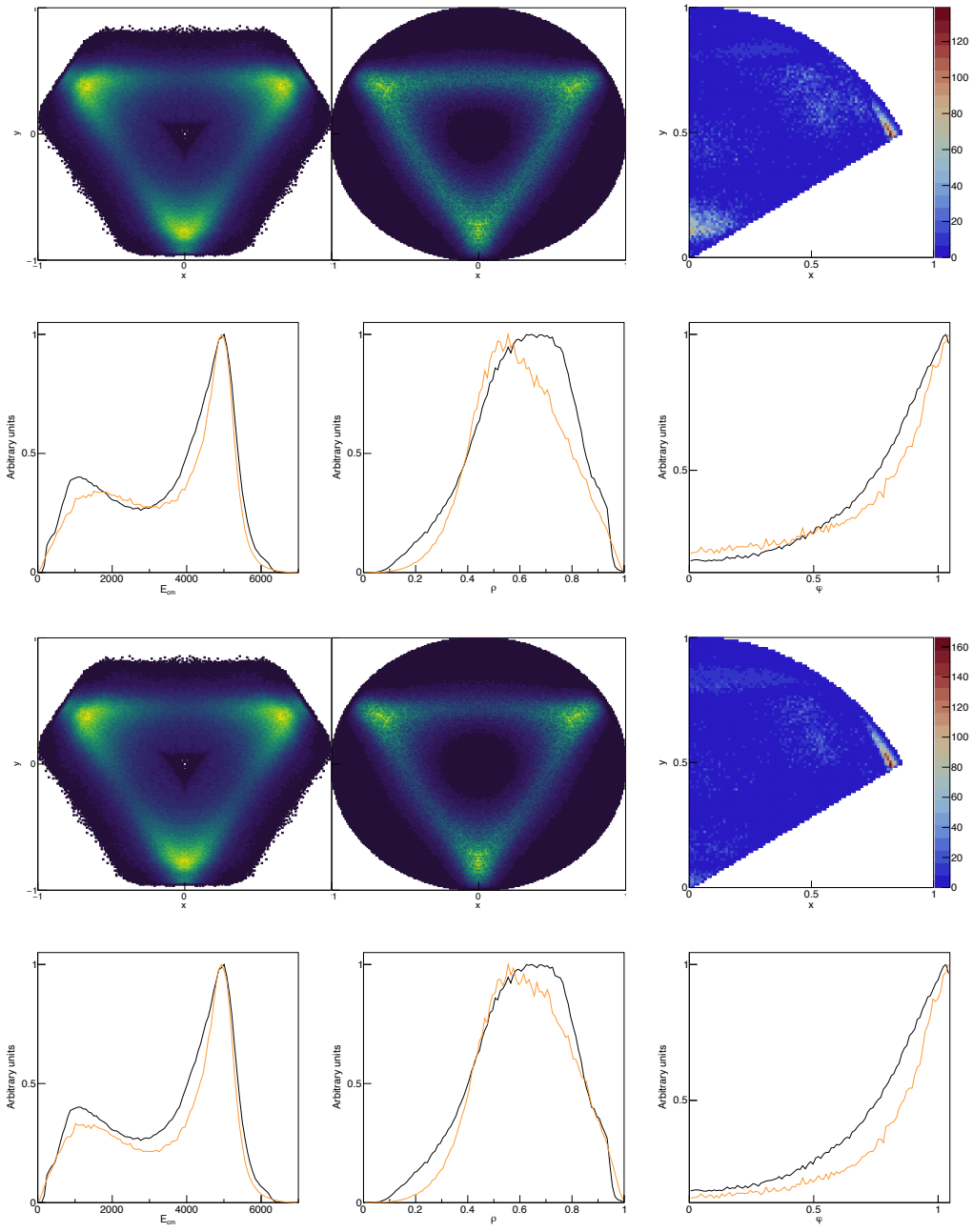

Figure 29: The top two rows shows the fit result of our 0^+ multiplicity 3 data with a simulated $\{2_1^-, 2_3^-\}$ state. The bottom two rows similarly shows the fit of a simulated $\{2_1^-, 2_3^-\}$ and $\{3_1^-, 3_3^-\}$ state. For the fit values, see table 7.

By visually comparing the Dalitz plots of the fit, we can already tell that this is a far better fit than the pure 0^+ simulations from figure 20. Based on

the projections, the fit is in surprisingly good agreement with our data, as we already suspected would be the case based on the correlation angle fits. Although it is a good match, it is by no means perfect: if we look at the binwise χ^2 distribution (top right corner), there are still some issues near the center and edge. The reason this plot is only a slice is because that is what the fitter actually fits internally, and the full plots are simply reconstructed based on the result of this.

Since there is still room for improvement, a series of additional fits were performed, all of which are listed in table 7. The fit with both the 2^- and 3^- states were repeated with 3^-_1 and 3^-_3 individually, in an attempt to see if reducing the parameter space would give better results. It is interesting that the fit allowing for a 0^+ component finds no trace of the state in the data, in agreement with the correlation angle analysis. Since this fit is based on the entire Dalitz plot, the minor deviations in the phase-space densities near the edge can no longer be used as an excuse for its absence. The best result which could be found is a mixture of 2^- and 3^- states, which are also shown as the bottom two rows in figure 29. Visually there is no real difference between the Dalitz plots, and similarly no significant change in the projections can be seen. Only the binwise χ^2 distribution can really tell us what has changed: the additional 3^- state corrects the low-count area near the center. Except for a major deviation near the edge, this fit would appear to be nearly perfect. We will return to the discussion of these edge deviations later. The fitted 2^- parameters are drastically different from those obtained through the other fits, which were otherwise consistent. What is even more interesting about them is that they are incredibly similar to those found for the nearby 16.62 MeV 2^- resonance, whose fitted parameters can also be found in the table. However, with a width of just 280(28) keV [15], this 2^- resonance is more than four full widths away from the 17.76 MeV resonance, and so it is most likely not due to interference from this state.

All of the fits were repeated for all of our available data, i.e. both multiplicity 2 and 3. We have earlier seen clear traces of protons in the filtered multiplicity 2 data, and to avoid these areas in the fit, they were simply removed with an aggressive cut of $y = 0.85$. Despite this, the fits are generally quite poor, which would indicate that our efforts are not enough to completely remove the proton contaminated data. Although these fits are not that informative due to their issues, it is worth noting that the fit is particularly bad when using only a 2^- simulation. Furthermore, it also finds the $l = 3$ component to be dominating, which is unphysical due to the angular momentum barrier. Since this fit is exceedingly poor with only a 2^- component, but is dramatically

improved by the addition af any other state, it somewhat supports our best multiplicity 3 fit with both a 2^- and 3^- state.

5.4.2 2^-

We have already briefly talked about the 2^- fits, which will be expanded upon here. Figure 22 shows its projections, which are all extremely good matches.

As was also mentioned earlier, Kuhlwein [9] looked at the exact same data, and found very similar results, as can be seen in table 5. Although they used a cut on the y-axis, this proved to be unnecessary for us since we already filtered the ground state decays through the E_{2-3} energies. As was already mentioned in the table, we can get even better results by accounting for the Coulomb interaction between the primary and secondary particles, which is neglected in (29). The basic idea is that when a secondary particle is emitted in a similar direction as the primary, and has sufficiently high energy, it can overtake it. Due to their proximity, they will interact strongly through the Coulomb interaction. A basic way of accounting for this would be to simply introduce extra barrier penetrabilities in the equation, one for each of the two secondary particles [25].

This Coulomb repulsion should affect primarily the areas of the Dalitz plot with a small angle between the primary and secondary particles. If we look back at figure 2, these are the areas near the edge of the Dalitz plot, which is exactly where our fits are struggling (see the binwise χ^2 plots on figures 29 and 30). Kuhlwein's analysis *does* account for this effect, which dramatically improves their fits to a χ^2 value of just 9165, a reduction of roughly 30%. Compare this with our best estimates in table 7. Based on their binwise χ^2 plots, it appears as if this correction primarily targets the edges of the Dalitz plots, as we already anticipated. Thus it is believed that a similar improvement can be made with the 0^+ fits by accounting for this effect, but due to time constraints, this could not be implemented.

The multiplicity 2 data were generally far cleaner than it was for the 0^+ and 3^- data, which is most likely due to the lower beam energy. Thus no cut on the y-axis was necessary when fitting to it. As we also found for the 0^+ data, using both multiplicities results in a worse fit than when we use only multiplicity 3. In contrast to the discussion we made there, the two fits are here in rough agreement with their findings, no matter what data we use.

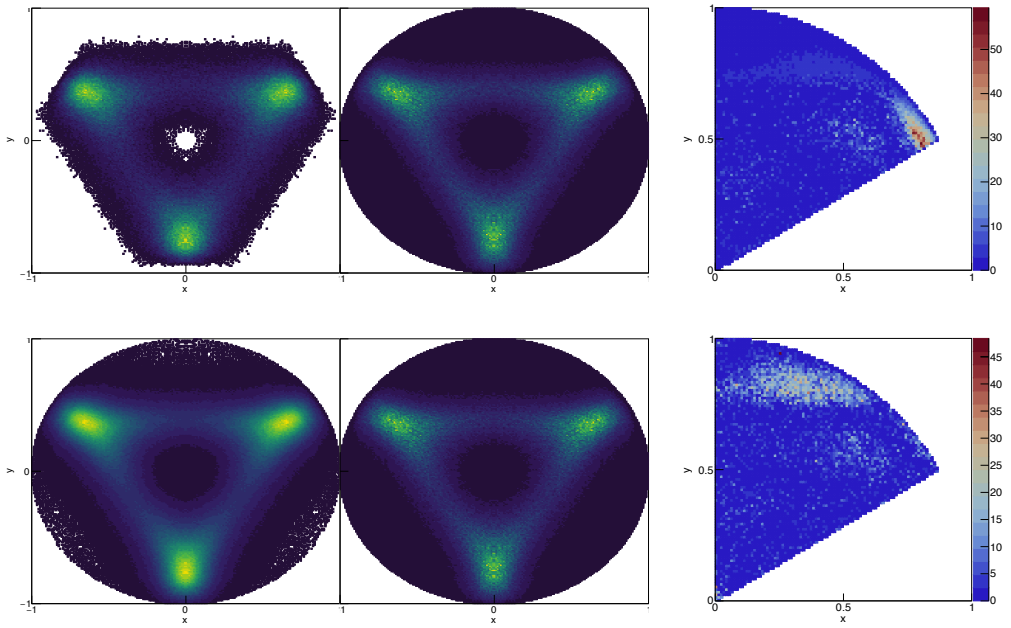

Figure 30: The top row shows the fit result of our 2^- multiplicity 3 data with a simulated $\{2_1^-, 2_3^-\}$ state. Similarly the bottom row shows the fit of both our multiplicity 2 and 3 data to the same simulation. For the projections of the former, see figure 22. For the fit values, see table 7.

5.4.3 3^-

Finally, since we have the data available anyway, a fit was made to the 3^- data as well. The goodness-of-fit is similar to that of the 2^- state, as can be seen in table 7. The results of this fit can be found in figure 31. Clearly something is not quite right with the simulated Dalitz figure - the line segments never quite merge into one, as they should. This gives rise to the large χ^2 deviation near the vertex, which may also be partly due to Coulomb repulsion. To see that this is not an issue with the fit itself, the Dalitz plots of the pure simulations 3_1^- and 3_3^- can be seen on figure 35 in the appendix. Both of these share this feature, and are thus not capable of describing the data alone.

A likely explanation for this difference is that we are using a wrong reduced width amplitude γ in our simulations. If we look back at figure 24, we see that as this width increases, the interference between the bands becomes stronger, especially near the vertices and in the center. This would almost perfectly account for the visual difference between the two plots. It is hard to judge what effect this would have on the projection plots. As already

mentioned, the area is also in the Coulomb repulsion zone, which could also be the culprit. A third explanation could be that we are seeing effects from the tail end of the second excited state of ^{8}Be*. This 4^+ resonance has an energy of 11 350 keV, but is very broad, with a width of 3.5 MeV [15], and could thus have some subtle effects on our plots.

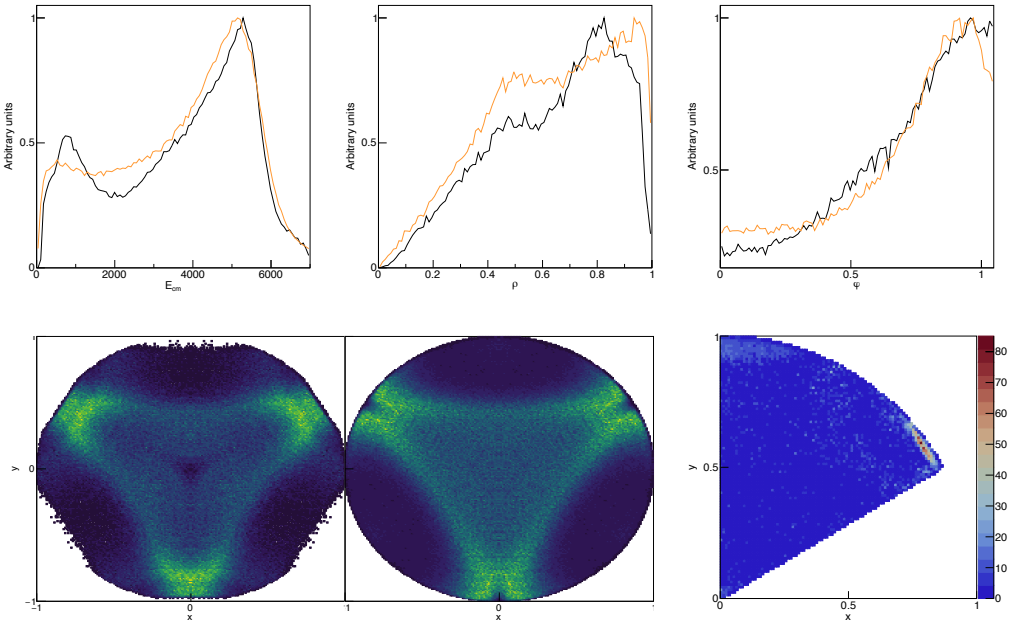

Figure 31: The fit result of our 3^- multiplicity 3 data with a simulated $\{3^-_1, 3^-_3\}$ state. For the fit values, see table 7.

In an attempt to improve the fit further, a series of extra fits were made to the same data. No real improvement could be found, although quite a few different combinations results in fits that were just as good as the single 3^-. Without any further evidence for their existence, it is hard to argue why any of these should be favored over the simpler option. Similarly to the 0^+ data, the fits were repeated for all our data, i.e. both multiplicity 2 and 3. For much the same reasons, an aggressive cut of $y = 0.85$ was imposed on the data, such as to avoid the most obvious proton-contaminated areas (see figure 37 in the appendix). In line with the other data sets, these fits are generally somewhat worse than when using only multiplicity 3 data. Once again the explanation for this is probably that there is still quite a few random proton coincidences which has managed to survive our cuts.

There were some major issues with the E_{2-3} energies for the reconstructed data. The plot can be found in figure 36 in the appendix, where four individual peaks can be identified. It is believed that the two additional peaks are due to protons, where the peaks have been shifted around because the equation for E_{2-3} assumes that they are α-particles. With these extra peaks present, the result of any fit using this data becomes dubious at best. Thus, as we have already discussed several times, we should really only trust the clean multiplicity 3 data. As was also the case for the 2^-, but not for the 0^+, the fits using both multiplicities roughly agrees with those using only multiplicity 2.

Data	Multiplicity	Simulation 1	Simulation 2	χ^2	dof	k_1	δ_1 [2π]	c	k_2	δ_2 [2π]
0^+	3	$2_1^-, 2_3^-$		29 561	5341	7.86(2)%	66.9(1)%			
	3	$2_1^-, 2_3^-$	0_2^+	29 516	5321	7.87(2)%	66.9(1)%	1 (1e-5)		
	3	$2_1^-, 2_3^-$	3_1^-	26 823	5344	8.95(3)%	66.3(1)%	0.916(2)		
	3	$2_1^-, 2_3^-$	3_3^-	29 381	5324	7.26(2)%	67.3(2)%	0.986(1)		
	3	$2_1^-, 2_3^-$	$3_1^-, 3_3^-$	25 230	5341	22.0(6)%	66.2(1)%	0.811(4)	37(1)%	27.6(3)%
	both	$2_1^-, 2_3^-$		111 408	4779	90.9(1)%	8.22(8)%			
	both	$2_1^-, 2_3^-$	0_2^+	31 049*	4748	50%	63.3%	0.771		
	both	$2_1^-, 2_3^-$	3_1^-	36 263*	4774	99.3%	12.4%	0.703		
	both	$2_1^-, 2_3^-$	3_3^-	37 344	4750	78.6(4)%	83.1(2)%	0.574(2)		
	both	$2_1^-, 2_3^-$	$3_1^-, 3_3^-$	39 332*	4772	97.4%	1.81%	0.709	56.8%	9.26%
2^-	3	$2_1^-, 2_3^-$		13 453	5347	19.8(5)%	67.4(2)%			
	both	$2_1^-, 2_3^-$		16 205	5347	20.9(3)%	67.82(8)%			
3^-	3	$3_1^-, 3_3^-$		13 691	5337	11.3(6)%	62.1(3)%			
	3	$3_1^-, 3_3^-$	2_1^-	12 314	4954	6.81(7)%	65.9(7)%	0.90(1)		
	3	$3_1^-, 3_3^-$	2_3^-	12 375	5098	10.0(6)%	63.6(3)%	0.865(6)		
	3	$3_1^-, 3_3^-$	$2_1^-, 2_3^-$	13 180	5339	15.1%	63.0%	0.886	92.5%	75.9%
	both	$3_1^-, 3_3^-$		21 826	4778	6.3(4)%	57.9(3)%			
	both	$3_1^-, 3_3^-$	2_1^-	18 961	4551	9.6(4)%	61.4(2)%	1(1e-4)		
	both	$3_1^-, 3_3^-$	2_3^-	18 901	4611	6.7(4)%	64.2(2)%	0.804(4)		
	both	$3_1^-, 3_3^-$	$2_1^-, 2_3^-$	20 112	4773	15.1%	61.4%	0.848	87.9%	82.9%
0^+	3	$2_1^-, 2_3^-$	$3_1^-, 3_3^-$	29 639	5340	0.79(6)%	0 (fixed)	0.931(2)	1.8(6)	0 (fixed)
2^-	3	$2_1^-, 2_3^-$		15 951	5347	14.0(5)%	0 (fixed)			
3^-	3	$3_1^-, 3_3^-$		14 405	5337	0(2e-14)%	0 (fixed)			

Table 7: The results of various fits performed with the Dalitz fitting tool. A (*) indicates the found minimum is poor, meaning the errors could not be estimated. All errors are purely statistical. The k values are always the ratio of ($l = 3$) to ($l = 1$), while c is the ratio of (Simulation 1) to (Simulation 2).

5.4.4 The δ parameter

So far we have let the additional relative phase difference between the two partial waves, δ, be a free parameter in all of the fits. As was mentioned when it was first introduced, this parameter is a crude attempt at describing a possible divergence from the purely sequential theoretical expressions, which ideally should be equal to zero. From table 7 we see that in *no* cases were this parameter equal to zero, and is in most cases substantially different. It would thus be interesting to redo some of these fits with this additional relative phase being locked to 0 as a fixed parameter. Only the best fit for each data set was repeated, and only for multiplicity 3 data. The results are listed at the bottom of table 7. Although the difference in χ^2 is not particularly large, only the ratios of the 2^- fit somewhat agrees with what we found when including δ. The other two completely removes the $l = 3$ components, which does not make much physical sense - we would expect at least some small component to be present. For the 0^+ and 3^- fits, this is supported by the visually poor Dalitz plot matches, which can be seen in figure 32.

Based on this evidence, it would appear as if this additional phase is necessary and actually has a substantial value. This would imply that an important piece of the interaction is unaccounted for in the purely sequential description provided by equation (30). In the analysis by Kuhlwein [9] the δ values only changes slightly depending on if the Coulomb repulsion is accounted for or not. Thus it would imply that there are still important interaction effects beyond this repulsion present in the data.

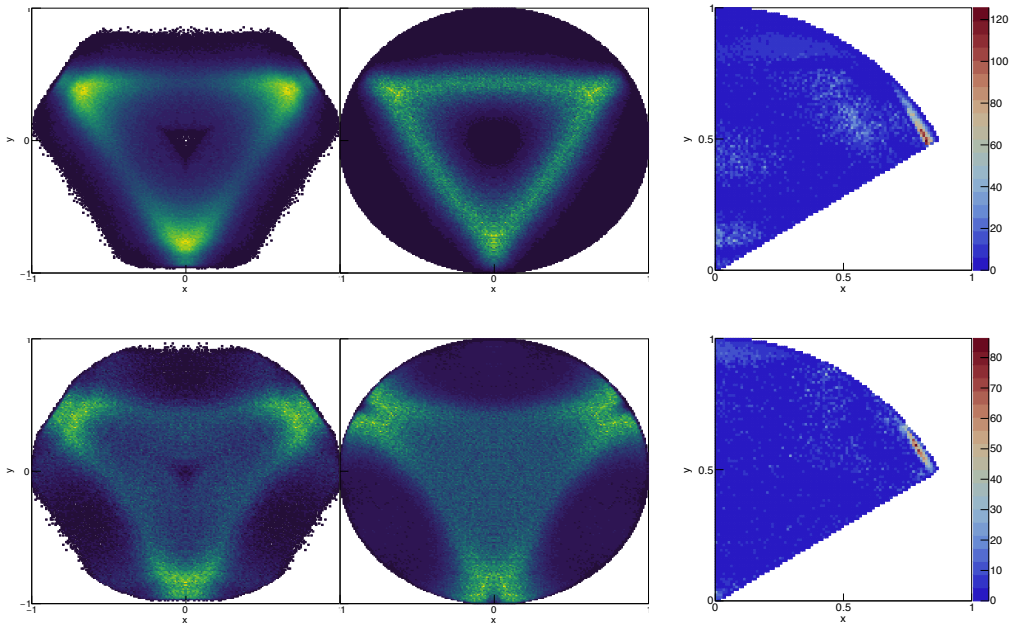

Figure 32: The top (bottom) row shows the results of fitting the multiplicity 3 0^+ (3^-) data with the relative phase δ fixed to 0.

5.5 Discussion

The main goal of this thesis was to perform a detailed analysis of the 17.76 MeV resonance, which is now finished. Since we have used quite a few different methods and obtained a lot of results, we will in this section briefly restate and discuss the most important ones.

Our very first estimate of the 0^+ contribution was based on the relative number of events on the two bands α_0 and α_1. Here we found that in the best-case scenario, we could expect either 39% or 79%, depending on if we follow Symons [11] or Segel [12]. We have already argued that in all of our results, we should only really trust our multiplicity 3 data, since the multiplicity 2 data appears to contain a substantial number of protons. This does not mean that they are completely useless, only that we should not expect to get exact values from its fits. With this in mind, our angular correlation analysis could not decisively rule out a possible minor 0^+ contribution to the data. Although both approaches (i.e. using the α or β angle) did not find any trace of a 0^+ contribution, we argued that this may be due to an inherent bias in the angular correlation distributions. It is certain, however, that any such contribution would be minor at best. Although we found the $l = 1$

and $l = 3$ components to be about equal, due to their large uncertainties, we cannot really say anything further about those. Thus the main takeaway of this step of the analysis was that the level is dominated by a 2^- resonance.

We then took this result one step further, and performed a Dalitz-plot fit of our 0^+ data to a 2^- simulation. The results of this was surprisingly good, but could be further improved by also allowing a small 3^- component. We also found absolutely *no* trace of a 0^+ component, which cannot be explained by bias effects. Furthermore, the uncertainties are extremely small on this component, indicating that it is a poor representation of our data. We already saw this visually when we initially compared a pure 0^+ simulation to our data. Thus this analysis decisively tells us that any possible 0^+ contribution to the α_1 band must be vanishingly small. We also fitted our data from the 16.62 MeV and 18.35 MeV resonances with their respective simulations. The former is in exceedingly good agreement, while the latter was only decent. We argued that the reason for this was a poor choice of R-matrix parameter values. Nonetheless, this latter fit does not explicitly disagree with the 3^- assignment, although it is dubious how accurate the fitted ratio between the partial wave contributions is.

Based on the analysis performed in this thesis, we can thus conclude that the α_1 band of the 17.76 MeV level is dominated by a 2^- resonance. This is in clear disagreement with previous research which has shown that the level is also resonant on the α_0 band, which means that it must have natural parity [11][12][14]. These studies are all based on a Legendre-series fit of the angular correlation distributions, and thus one possible resolution to this disagreement could be that there are *two* resonances around this level. The previously observed 0^+ resonance could then dominate the α_0 band, while the 2^- resonance could dominate the α_1 band. This resolution is not very satisfactory, however, since neither Symons, Segel or Hanna [13] noted any such possibility.

We also measured the ratio of the partial widths Γ_{α_0} and Γ_{α_1} for both the 17.76 MeV and 18.35 MeV resonances. The result for the latter nicely agrees with the literature, while the former does not. However, both Symons and Segel mentions that they found two possible solutions that fit their measured cross sections. Symons prefers the lower value which agrees with our measurement, while Segel prefers a higher value which has since been adopted by the NNDC. However, Segel also mentions that a computation error was discovered in Symons calculation of the higher value, citing a private communication. Whether this also extends to the lower value we have used here

is unknown.

One of our main tools in this analysis was the Dalitz fitter. This tool was not without its issues however, since it neglects the Coulomb repulsion and includes an additional relative phase difference δ between the partial waves. Furthermore, this extra parameter does not vanish, as we would expect it to. This indicates that there are still other interactions which are unaccounted for. Thus to obtain better agreement with our data, we will most likely need a proper three-body model.

6 Conclusion

We have in this thesis primarily focused on the α_1 band decays of the ^{12}C 17.76 MeV resonance. We also applied the main parts of our analysis to the 16.62 MeV and 18.35 MeV resonances; the former to validate our tools and replicate the results of Kuhlwein [9], and the latter since we had the data on hand anyways.

The results from both the Dalitz-plot and angular correlation analysis of the 17.76 MeV resonance are in agreement: the level is dominated by a 2^- resonance. This is in direct disagreement with the 0^+ assignment of the resonance as found by multiple previous studies [11][12][13][14]. Our most powerful tool, the Dalitz-plot fitter, found *no* trace of this state in our data. No satisfactory explanation for this difference could be found. Our result for the ratio $\Gamma_{\alpha_0}/\Gamma_{\alpha_1}$ is in agreement with Symons [11], but disagrees with the commonly adopted value found by Segel [12].

Our results for the 2^- resonance agrees with [9], as long as the Coulomb interaction between the final α particles is neglected. The analysis of the 3^- resonance is inconclusive, since our simulations cannot possibly fully replicate the data. It is believed that this issue can be solved by fine-tuning the R-matrix parameters. Our result for the ratio $\Gamma_{\alpha_0}/\Gamma_{\alpha_1}$ is in agreement with both Symons and Segel. In particular it is worth noting that our analysis does not disagree with the 2^- and 3^- assignations of the 16.62 MeV and 18.35 MeV resonances.

References

[1] M. Oliphant, L. Rutherford, Proceedings of the Royal Society of London. Series A, Mathematical and Physical Sciences **141**, 259 (1933)

[2] P. I. Dee, C. W. Gilbert, Proceedings of the Royal Society of London. Series A, Mathematical and Physical Sciences **154** 881, 279 (1936)

[3] F. Hoyle, Astrophysical Journal Supplement, **1**, 121 (1954)

[4] D. N. F. Dunbar, R. E. Pixley, W. A. Wenzel, W. Whaling, Phys. Rev. **92**, 649 (1953)

[5] G. A. P. Cirrone et al, Scientific Reports **8**, 1141 (2018)

[6] J. L. Quebert, L. Marquez, Nucl. Phys. A **126**, 646 (1969)

[7] H. W. Becker, C. Rolfs, H. P. Trautvetter, Zeitschrift für Physik A Atomic Nuclei **327**, 341 (1987)

[8] S. Stave et al. Physics Letters B **696.1**, 26 (2011)

[9] M. Kuhlwein, Aarhus University (2020)

[10] H. E. Gove, E. B. Paul, Phys. Rev. **97**, 104 (1955)

[11] G. D. Symons, P. B. Treacy, Nucl. Phys. **46**, 93 (1963)

[12] R. E. Segel, S. S. Hanna, R. G. Allas, Phys. Rev. **139**, B818 (1965).

[13] S. S. Hanna, W. Feldman, M. Suffert, D. Kurath, Phys. Rev. C **25**, 1179 (1982)

[14] M. Munch, O. S. Kirsebom, J. A. Swartz, H. O. U. Fynbo, The European Physical Journal A, **56**, 17 (2020).

[15] NuDat 2.8, a database of nuclear information by the National Nuclear Data Center.
URL: www.nndc.bnl.gov/nudat2

[16] N. Bohr, Nature **137**, 344 (1936)

[17] V. Weisskopf, E. Wigner, Z. Physik **63**, 54 (1930)

[18] Lecture notes from D. Baye, one of the authors of [20]. This is essentially just a simplified version of his review paper.
URL: nucleartheory.eps.surrey.ac.uk/Talent_6_Course/Other_materials/lectures/Trento_Baye_Rmatrix.pdf

[19] C. Bloch, Nucl. Phys. **4**, 503 (1957)

[20] P. Descouvemont, D. Baye, Rep. Prog. Phys. **73**, 036301 (2010)

[21] G. G. Ohlsen, Nucl. Instrum. Methods **37**, 240 (1965)

[22] R. H. Dalitz, The London, Edinburgh, and Dublin Philosophical Magazine and Journal of Science, **44:357**, 1068-1080 (1953)

[23] A. Wuethrich, arXiv:hep-ph/0507058 (2005)

[24] C. Zemach, Phys. Rev. **133**, B1201 (1964).

[25] H. O. U. Fynbo et al., Phys. Rev. Lett. **91**, 082502 (2003)

[26] L. C. Biedenharn, M. E. Rose, Rev. Mod. Phys. **25**, 729 (1953)

[27] *Nuclear Physics of Stars*, Christian Iliadis (2007)

[28] J. Beringer et al. (Particle Data Group), Phys. Rev. D **86**, 010001 (2012). Chapter 36 on statistics.

[29] R. Barlow, C. Beeston, Computer Physics Communications **77.2** (1993)

[30] O. S. Kirsebom, Aarhus University (2010)

[31] S. Baker, R. D. Cousins, Nucl. Instrum. Methods in Physics Research, **221.2**, 437 (1984)

[32] ROOT, a C++ data analysis framework.
URL: root.cern.ch

[33] AUSAlib, a C++ data analysis framework built on top of ROOT.
URL: gitlab.au.dk/ausa/ausalib/-/wikis/home

[34] ucesb, the unpacking tool utilized internally in AUSAlib.
URL: fy.chalmers.se/~96hajo/ucesb

[35] J. F. Ziegler, M. D. Ziegler, J. P. Biersack, Nucl. Instrum. Methods B 268, 1818 (2010)

[36] A. M. Lane, R. G. Thomas, Rev. Mod. Phys. **30**, 257 (1958)

[37] D. P. Balamuth, R. W. Zurmühle, S. L. Tabor, Phys. Rev. C **10**, 975 (1974)

[38] The *Genetic* algorithm implemented by `ROOT`.
`URL`: root.cern.ch/download/doc/tmva/TMVAUsersGuide.pdf#page=65

[39] The `MINOS` tool from `ROOT` for identifying errors.
`URL`: https://root.cern.ch/download/minuit.pdf#page=10

[40] M. Bhattacharya, E. G. Adelberger, H. E. Swanson, Phys. Rev. C **73**, 055802 (2006)

[41] mpmath, a Python library which provides easy access to the Coulomb wave functions. `URL`: https://mpmath.org/

[42] SymPy, a Python library containing countless obscure functions and symbols. `URL`: https://www.sympy.org/en/index.html

A Supplementary calculations

A.1 Deriving the shift and penetrability factors

The starting point for these calculations is the Wronskian relation satisfied by the Coulomb functions F_l and G_l

$$F_l' G_l - G_l' F_l = 1$$

Starting from the definition of L_l, and remembering that $I_l = G_l - iF_l$ and $O_l = G_l + iF_l$, we can now derive the expressions for S_l and P_l

$$\begin{aligned}
L_l &= \rho \frac{O_l'}{O_l} \\
&= \rho \frac{G_l' + iF_l'}{G_l + iF_l} \\
&= \rho \frac{G_l' + iF_l'}{G_l + iF_l} \frac{G_l - iF_l}{G_l - iF_l} \\
&= \rho \frac{G_l' G_l + F_l' F_l + i(G_l F_l' - F_l G_l')}{G_l^2 + F_l^2} \\
&= \rho \frac{G_l' G_l + F_l' F_l}{G_l^2 + F_l^2} + i \frac{\rho}{G_l^2 + F_l^2} \\
&= S_l + iP_l
\end{aligned}$$

A.2 Basic kinematics

A.2.1 The energies of each particle

The goal here is to derive the expressions for the energy of each particle in a two-step sequential decay, (16) to (18).

Since it is a sequential decay, we will analyze it in steps. For the first step we have no preferred direction in space, and so we can freely pick our x-axis to align with the directions of motion after the first decay. With this choice, then in the center-of-mass frame momentum conservation gives us (defining the pure indices 1, 2 & 3 as the α-particles) $p_1 + p_{Be} = 0$. By now noting that $E = p^2/2m$ and imposing energy conservation, we get

$$Q_1 = E_1 + E_{Be} = E_1 + \frac{(p_{Be}^x)^2}{2(2m_\alpha)} = E_1 + \frac{1}{2}\frac{(-p_1^x)^2}{2m_\alpha} = E_1 + \frac{1}{2}E_1 = \frac{3}{2}E_1$$

Solving for E_1, we arrive at the first equation

$$E_1 = \frac{2}{3}Q_1 \qquad\qquad E_{Be} = \frac{1}{3}Q_1$$

Now for the second decay. Since we have already defined our coordinate system, the calculations become slightly more tedious. In the ^{8}Be frame (denoted by primes), since the masses of the decay products are now equal, momentum conservation states that $\boldsymbol{p}'_2 = -\boldsymbol{p}'_3$. This trivially translates to $E'_2 = E'_3$, which, when combined with energy conservation, tells us that $E'_2 = Q_2/2$. By now boosting this result to the center-of-mass frame, we get the second equation

$$\begin{aligned}
E_2 &= \frac{1}{2}m_\alpha(v' + v_{Be})^2 \\
&= E'_2 + \frac{1}{2}E'_{Be} + m_\alpha v' v_{Be} \\
&= \frac{1}{6}Q_1 + \frac{1}{2}Q_2 + m_\alpha \cos\theta \sqrt{\frac{2E'_2}{m_\alpha}}\sqrt{\frac{2E'_{Be}}{2m_\alpha}} \\
&= \frac{1}{6}Q_1 + \frac{1}{2}Q_2 + \cos\theta \sqrt{\frac{2Q_2}{2}\frac{2Q_3}{6}} \\
&= \frac{1}{6}Q_1 + \frac{1}{2}Q_2 + \cos\theta \sqrt{\frac{Q_1 Q_2}{3}}
\end{aligned}$$

Through energy conservation in the center-of-mass frame, we have the relation $E_{Be} + Q_2 = E_2 + E_3$. By now solving for E_3, we can easily obtain the third equation

$$\begin{aligned}
E_3 &= E_{Be} + Q_2 - E_2 \\
&= \frac{1}{3}Q_1 + Q_2 - (\frac{1}{6}Q_1 + \frac{1}{2}Q_2 + \cos\theta\sqrt{\frac{Q_1 Q_2}{3}}) \\
&= \frac{1}{6}Q_1 + \frac{1}{2}Q_2 - \cos\theta\sqrt{\frac{Q_1 Q_2}{3}}
\end{aligned}$$

A.2.2 The angle between the primary and secondary particles

We want to derive an expression for the angular correlation α between the primary and secondary particles in a three-body decay. Our starting point is equation (19), where we simply substitute in our Dalitz coordinates (22).

We will also need the relation $Q_1 = E_{tot}(y+1)/2$. Then

$$\begin{aligned}
2\cos\alpha &= \sqrt{\frac{3}{Q_1 Q_2}}(E_2 - E_3) \\
&= \sqrt{\frac{3(y+1)}{Q_1 Q_2}}(E_2 - E_3)\frac{xE_{tot}}{\sqrt{3}(E_2 - E_3)} \\
&= \frac{xE_{tot}}{\sqrt{Q_1 Q_2}} \\
&= \frac{xE_{tot}}{\sqrt{E_{tot}\frac{y+1}{2}(E_{tot} - E_{tot}\frac{y+1}{2})}} \\
&= \frac{x}{\sqrt{\frac{y+1}{2}(1 - \frac{y+1}{2})}} \\
&= \frac{x}{\sqrt{\frac{1}{4}(1-y^2)}} \\
&= 2\frac{x}{\sqrt{1-y^2}}
\end{aligned}$$

Thus we arrive at the final simple result

$$\cos\alpha = \frac{x}{\sqrt{1-y^2}}$$

B Figures

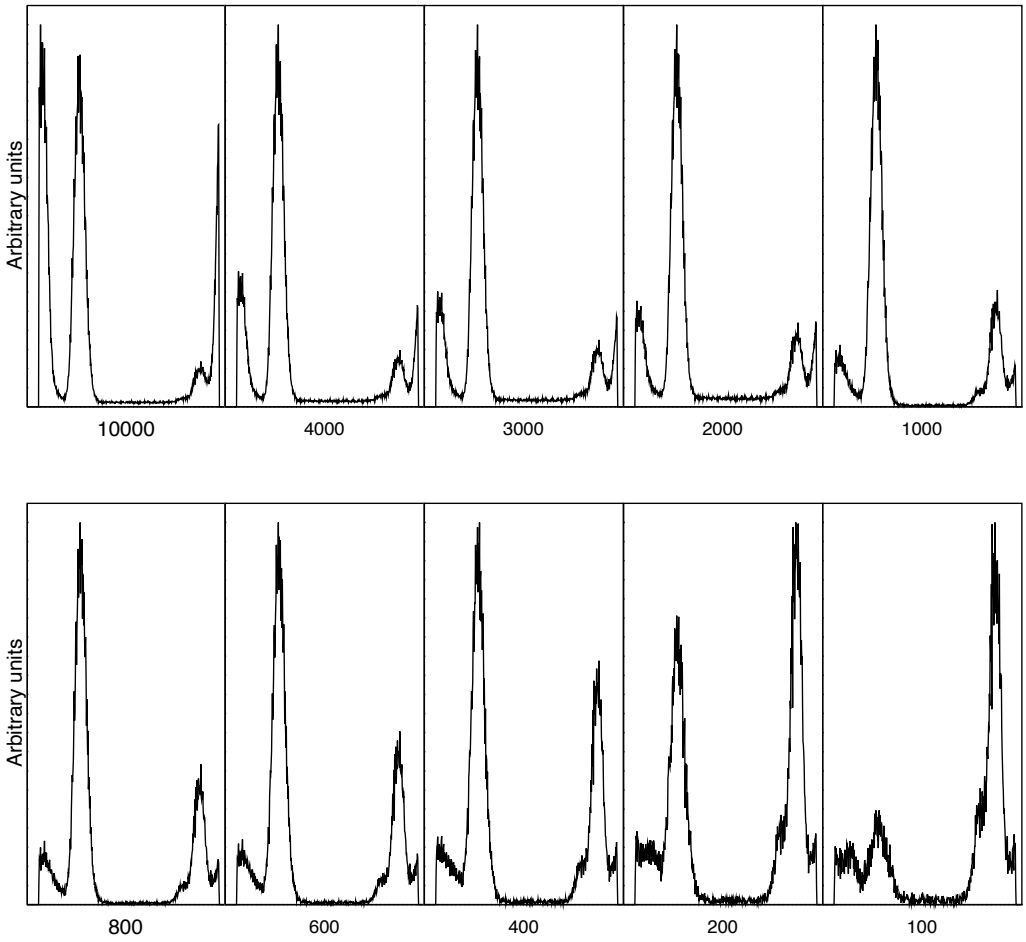

Figure 33: The energy dependency of the `TDC` peaks. The x-axis labels are the maximum energy E_α allowed in each panel in keV. Note how the middle peak contains primarily low-energy particles, and only starts to disappear around $E_\alpha \sim 300$.

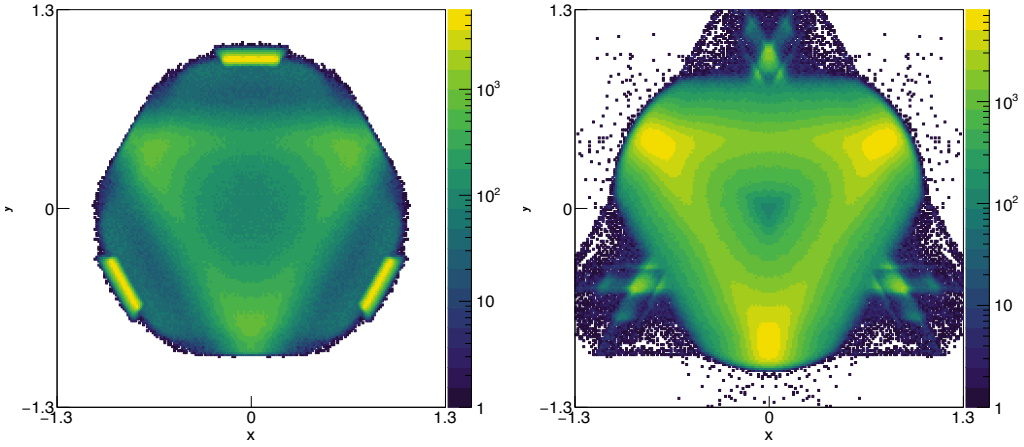

Figure 34: The raw, uncut Dalitz plots for the 0^+ data. The left panel shows the plot for our multiplicity three data, while the right shows it for the multiplicity two data. Note how the weird cones on the right panel extends well outside the energetically allowed region, which indicates that they are due to protons.

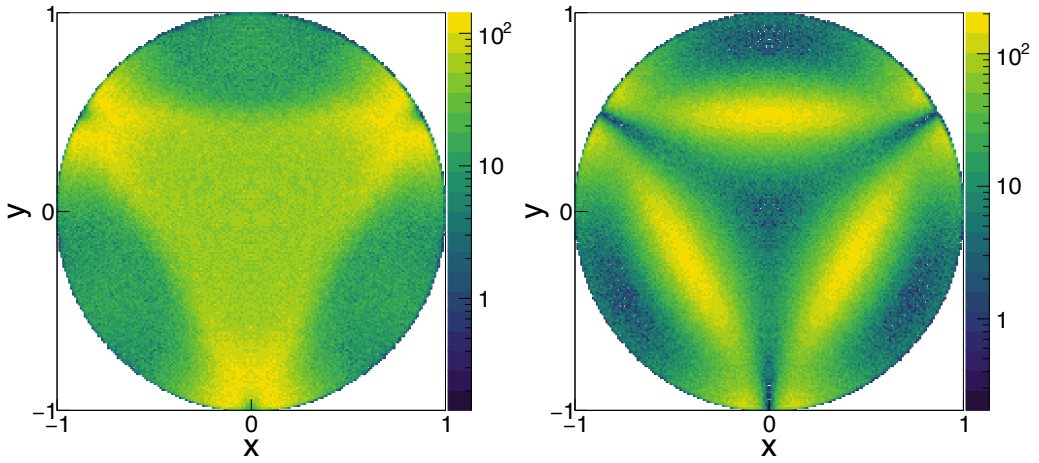

Figure 35: The Dalitz plots for a pure 3_1^- (left) and 3_3^- (bottom) simulation. Note the small area near the edge which is suppressed in both figures. Since our data does not share this feature, it means that these two simulations could never possibly describe it perfectly. In the text we attributed this to a wrong choice of R-matrix parameter values.

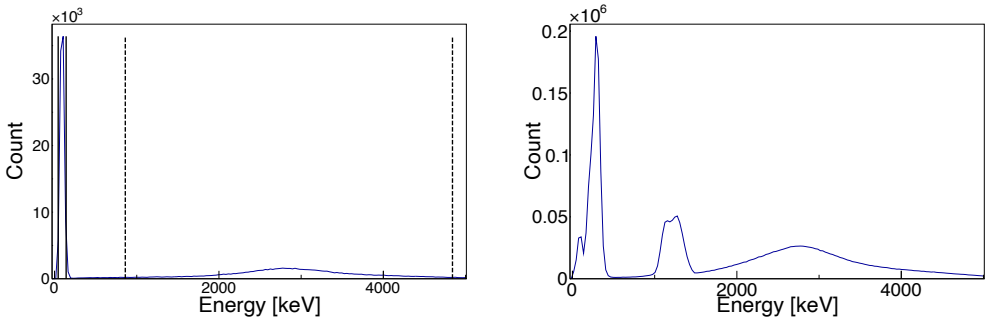

Figure 36: The left (right) panel shows the E_{2-3} energies of the multiplicity 3 (2) 3^- data. On the left panel, the solid black lines illustrates the 2σ borders of the α_0 peak, while the dashed lines similarly shows the α_1 borders. If the 3σ values are used instead, the intervals would overlap. On the right panel, multiple extra peaks are present. It is unknown where they originate from.

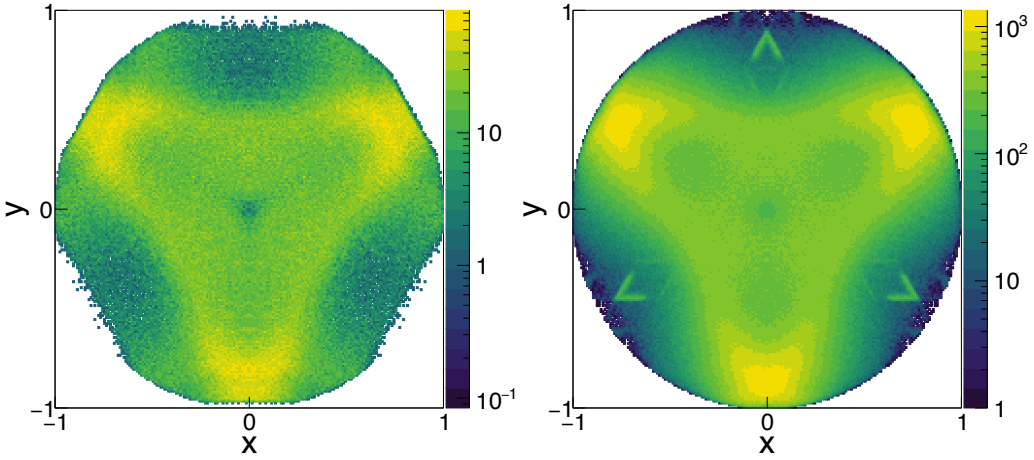

Figure 37: The Dalitz plots for the multiplicity 3 (left) and 2 (right) 3^- data. Note the similarity on the right panel to the cones on figure 34.

C Code

The scripts used for every part of the analysis can be found on my github which I used for the entire project: https://github.com/krellemeister/Speciale. The scripts themselves are located in the analysis/scripts/ directory.